CHEMISTRY & SUSTAINABILITY

CHEMSUSCHEM

ENERGY & MATERIALS

10/2017

Front Cover Picture:
Wang et al.
Nitrogen Fixation by Gliding Arc Plasma:
Better Insight by Chemical Kinetics Modelling

A Journal of
ChemPubSoc Europe

WILEY-VCH

www.chemsuschem.org

Nitrogen Fixation by Gliding Arc Plasma: Better Insight by Chemical Kinetics Modelling


Dr. Weizong Wang


Bhaskar Patil


Stjin Heijkers


Prof. Dr. Volker Hessel


Prof. Dr. Annemie Bogaerts

Universiteit Antwerpen

TU/e Technische Universiteit Eindhoven University of Technology

Invited for this month's cover is the group of Prof. Dr. Annemie Bogaerts at the University of Antwerp and their collaborators at Eindhoven University of Technology in the laboratory of Prof. Dr. Volker Hessel. The cover image shows that gliding arc plasma leads to energy efficient nitrogen fixation by promoting the vibrational excitation of N_2.
The Full Paper itself is available at 10.1002/cssc.201700095.

What prompted you to investigate this topic/problem?

Considering the increasing demand of fertilizers as well as the high-energy intensity and environmental concerns triggered by industrial nitrogen fixation (i.e., the Haber–Bosch process), there is an urgent need to develop and integrate more sustainable processes of nitrogen fixation. Gliding arc plasma-based nitric oxide synthesis offers unique perspectives for this purpose, but the underlying mechanisms are clearly not yet understood. Hence, we wanted to elucidate the plasma chemistry by a combination of experiments and computations, to provide the necessary insights for gliding arc plasma-based nitrogen fixation. Our work also allows us to propose possible solutions on how to further improve the performance of gliding arc plasma technology.

What is the most significant result of this study?

Our results clearly reveal that vibrational excitation of N_2 can help to overcome the reaction energy barrier of the non-thermal Zeldovich mechanism $O + N_2(V) \rightarrow NO + N$ and can thus significantly enhance the nitric oxide synthesis in the gliding arc plasma. This provides an energy efficient pathway for nitrogen fixation using air as raw material.

What future opportunities do you see (in the light of the results presented in this paper)?

If electricity from sustainable energy sources (wind and solar) is used, the intrinsic potential of gliding arc plasma-based nitrogen fixation can provide a promising opportunity for producing nitrogenous fertilizer in remote locations by just using small-scale plants, which offer farmers a new source of revenue from their land. This helps to come up with realistic scenarios of entering a cutting-edge innovation in new business cases of plasma agriculture, in which low-temperature plasma technology might play an important role.

Acknowledgements

The authors appreciate financial supports by the European Marie Skłodowska-Curie Individual Fellowship "GlidArc" within Horizon 2020 (Grant No.657304), the FWO project (Grant G.0383.16N) and the EU project MAPSYN: Microwave, Acoustic, and Plasma assisted SYNthesis (Grant No.CP-IP 309376) under the 7th Framework Programme. The calculations were performed using the Turing HPC infrastructure at the CalcUA core facility of the Universiteit Antwerpen (UAntwerpen), a division of the Flemish Supercomputer Center VSC, funded by the Hercules Foundation, the Flemish Government (department EWI) and the UAntwerpen.

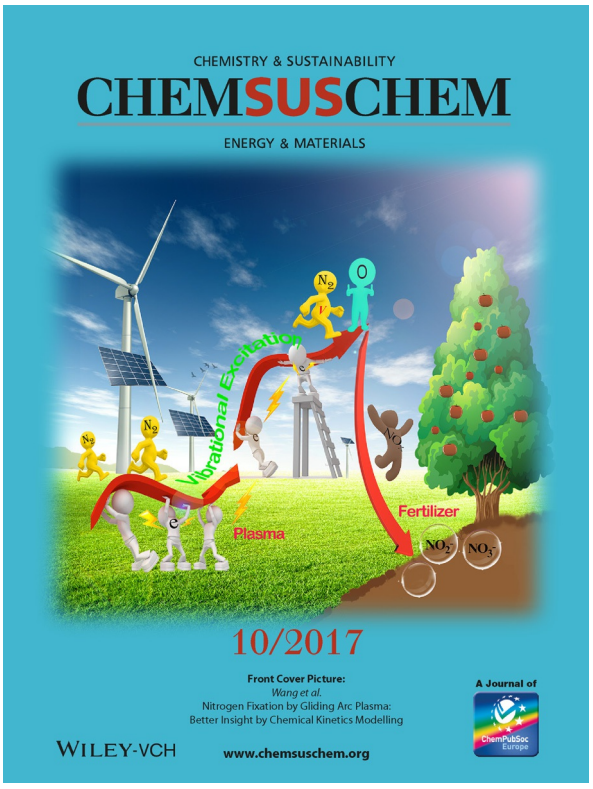

ChemPubSoc Europe

DOI: 10.1002/cssc.201700095

CHEMSUSCHEM Full Papers

VIP *Very Important Paper*

Nitrogen Fixation by Gliding Arc Plasma: Better Insight by Chemical Kinetics Modelling

Weizong Wang,*[a] Bhaskar Patil,[b] Stjin Heijkers,[a] Volker Hessel,[b] and Annemie Bogaerts*[a]

The conversion of atmospheric nitrogen into valuable compounds, that is, so-called nitrogen fixation, is gaining increased interest, owing to the essential role in the nitrogen cycle of the biosphere. Plasma technology, and more specifically gliding arc plasma, has great potential in this area, but little is known about the underlying mechanisms. Therefore, we developed a detailed chemical kinetics model for a pulsed-power gliding-arc reactor operating at atmospheric pressure for nitrogen oxide synthesis. Experiments are performed to validate the model and reasonable agreement is reached between the calculated and measured NO and NO_2 yields and the corresponding energy efficiency for NO_x formation for different N_2/O_2 ratios, indicating that the model can provide a realistic picture of the plasma chemistry. Therefore, we can use the model to investigate the reaction pathways for the formation and loss of NO_x. The results indicate that vibrational excitation of N_2 in the gliding arc contributes significantly to activating the N_2 molecules, and leads to an energy efficient way of NO_x production, compared to the thermal process. Based on the underlying chemistry, the model allows us to propose solutions on how to further improve the NO_x formation by gliding arc technology. Although the energy efficiency of the gliding-arc-based nitrogen fixation process at the present stage is not comparable to the world-scale Haber–Bosch process, we believe our study helps us to come up with more realistic scenarios of entering a cutting-edge innovation in new business cases for the decentralised production of fertilisers for agriculture, in which low-temperature plasma technology might play an important role.

Introduction

Nitrogen is an essential component for all forms of life because it is required to biosynthesise basic building blocks of plants and living organisms. The latter can consume nitrogen in a usable form, obtained by chemical reaction with oxygen or hydrogen or carbon. Therefore, we find nitrogen compounds in plant cells, amino acids, proteins and nucleic acids. In the earth's atmosphere, there is an abundant supply of nitrogen—78.08% of air is composed of molecular nitrogen (N_2). However, this most abundant nitrogen source is not available to the majority of living organisms because it is extremely difficult to break its triple bond and very stable electronic configuration, which makes almost any first reaction step of the conversion very energy demanding. As a result, nitrogen fixation (NF), which converts nitrogen molecules into simple nitrogen compounds, such as ammonia or nitric oxide that can be further used as precursors for the synthesis or biosynthesis of more complex molecules, is very significant. However, it is the most challenging step of nitrogen utilization by living organisms.[1]

The conventional Haber–Bosch (H–B) process of the binding of nitrogen with hydrogen to produce ammonia at high pressure and temperature is the most significant process to produce fertilisers.[2] It is expected that the global ammonia capacity will increase from 204.2 million tons per year in 2013 to 249.4 million tons by 2018.[3] Hence, the amount of synthetic nitrogen obtained by human activities has exceeded natural biological fixation.[4] From an energy point of view, industrial ammonia synthesis is the most energy intensive chemical process. The H–B process consumes 1–2% of the world's total energy production and utilises 2–3% of the total natural gas output. Furthermore, it emits more than 300 million metric tons of carbon dioxide.[5,6]

Considering the increasing demand of fertilisers, the high energy intensity and environmental concerns triggered by industrial NF (i.e., the H–B process), the need to develop and integrate more sustainable processes becomes imperative.[7,8] Several alternative (non-conventional) technologies are being investigated, such as biological NF,[9,10] and NF with metallo-complex homogeneous catalysts under ambient pressure.[11] Another new technology considered to have great potential for reducing the environmental impact and improving the energy efficiency is based on plasma, that is, an ionised gas, typically created by applying electric energy. Especially when sustainable energy sources such as wind and solar cells are utilised for the generation of electricity, the dependence on fossil

[a] *Dr. W. Wang, S. Heijkers, Prof. Dr. A. Bogaerts*
Department of Chemistry, research group PLASMANT
University of Antwerp
Universiteitsplein 1, 2610 Antwerp (Belgium)
E-mail: wangweizong@gmail.com
annemie.bogaerts@uantwerpen.be

[b] *B. Patil, Prof. Dr. V. Hessel*
Department of Chemical Engineering and Chemistry
Laboratory of Chemical Reactor Engineering/
Micro Flow Chemistry and Process Technology
Eindhoven University of Technology
P. O. Box 513, 5600 MB Eindhoven (The Netherlands)

Supporting Information and the ORCID identification number(s) for the author(s) of this article can be found under http://dx.doi.org/10.1002/cssc.201700095.

fuels during this industrial process is greatly reduced and no greenhouse gas emissions take place. This makes plasma an inherent "green" technology.

Plasma-based NF is generally accomplished by the reaction of nitrogen with oxygen or hydrogen to produce nitrogen oxide (nitric oxide) or ammonia, respectively.[1] For plasma-based ammonia synthesis, expensive hydrogen is required in addition to readily available nitrogen. In contrast, for plasma-based nitric oxide synthesis, the raw materials (air) are abundantly available at low cost. As a result, more research devoted to the plasma-based nitric oxide synthesis can be found in the literature.[12–16] For this purpose, either thermal or non-thermal plasma can be used. Thermal plasma, however, requires very high temperatures and the energy efficiency is low. Non-thermal plasma, on the other hand, is very promising because the theoretical limit of the energy consumption of nitrogen oxidation is more than 2.5 times lower than that of the H–B process.[16] Thus, atmospheric non-thermal plasmas offer unique perspectives because of their capacity to induce chemical reactions within gases with a limited energy cost at ambient pressure and temperature.

Gliding arc plasmas are among the most effective and promising plasmas for gas conversion[17–30] because they offer benefits of both thermal and non-thermal discharges. They are typically considered as "warm" discharges, and vibrational excitation of the molecules is seen as the most efficient way to assist the conversion or synthesis.[31] A few studies were reported on employing a gliding-arc reactor for NF.[32–38] The highest concentration of NO_x achieved was found to be 1.0% in a milli-scale gliding-arc reactor.[37] In this reactor, one can expect to benefit from an intensified contact of the reactive plasma species with the gas molecules, and therefore a higher efficiency in delivering energy to the reactant gases.

To improve the applications (i.e., mainly gas conversion), the physical and chemical characteristics of the gliding arc have been extensively studied experimentally.[39–44] Furthermore, computer modelling of the plasma chemistry and reactor design[45–59] is also very useful in providing more insight into the underlying reaction mechanisms of plasma-assisted gas conversion or synthesis, for example, by evaluating quantities that are difficult to measure, and by identifying the most important chemical reactions or parameters.[45–51] However, only a few papers in literature deal with modelling of a gliding arc.[52–59] To our knowledge, there exist no models yet for NO_x synthesis in a gliding arc.

Previous theoretical analysis revealed that vibrationally excited nitrogen plays an important role in energy efficient NO formation,[16,38] but these studies lack a description of the plasma chemistry. For N_2/O_2 mixtures, several papers presented kinetic models with a complex description of the vibrational and electronic levels,[60–64] but these models do not apply to a gliding-arc reactor. As a result, the various mechanisms that contribute to NO_x production in a gliding arc are not yet completely understood. This may be because a gliding arc is a non-stationary discharge and its effective volume changes due to the arc elongation caused by the gas blast. Therefore, building an accurate model for such a non-uniform reactor with a complex plasma chemistry is very challenging.

Herein, for the first time, we study the NO_x synthesis in a pulsed-power gliding-arc reactor by a chemical kinetics model. Experiments are performed to benchmark the model. More specifically, we compare the calculated and measured product yields of various NO_x compounds, the reaction selectivity and energy efficiency for different feed ratios of N_2/O_2. Moreover, by comparing these values with those for the pure thermal process, in which most of the energy is spent on the gas heating rather than on the nitrogen oxidation reactions, we can clearly demonstrate the non-equilibrium character of the gliding arc and explain the higher values of the NO_x yield and energy efficiency. Furthermore, to increase our general understanding of the underlying mechanisms and pathways, we perform a kinetic analysis, based on the simulation results, to elucidate the role of various plasma species, and especially of the N_2 vibrational states, in the NO_x synthesis. This enables us to propose solutions on how to further improve the formation of NO_x by gliding arc technology.

Results and Discussion

NO_x formation

The measured and calculated NO and NO_2 concentrations are plotted as a function of N_2/O_2 ratio in the gas mixture in Figure 1a,b. The total NO_x concentration (i.e., sum of $NO + NO_2$) and the NO and NO_2 selectivity are presented in Figure 2a,b.

Note that the experiments are limited to a N_2/O_2 ratio in the range of 0.25–4, whereas the simulations are performed in a wider range of 0.025–40 to obtain additional information. The concentrations of NO and NO_2 follow a similar parabolic trend upon varying the N_2/O_2 ratio, and there is an optimum feed ratio at which the maximum yield is reached. This is logical, because both N_2 and O_2 are the (initial) precursors for NO and NO_2. In the experiment, the concentration of NO increases until a feed ratio of 3 after which the NO concentration starts to decline. The NO_2 concentration reaches its peak at a feed ratio of 1. The calculated results follow a left-skewed trend for both NO and NO_2, as well as for their sum, with respect to the experimental values. However, the absolute values of the calculated and measured concentrations are in rather good agreement, certainly in view of the complexity of the plasma chemistry.

At a feed ratio of N_2/O_2 around 1, both the NO and NO_2 selectivity are close to 50%, but at a higher feed ratio, both the experimental and calculated NO selectivity increase, whereas the NO_2 selectivity shows the opposite trend. This is logical, because NO_2 production by NO oxidation becomes less important upon increasing fraction of N_2. When the feed ratio of N_2/O_2 is below 1, the NO selectivity again increases slightly, and the calculated value reaches about 60% at a low N_2/O_2 ratio around 0.02, whereas the calculated NO_2 selectivity is only 40%. This is because the net formation rate of NO_2 decreases more than that of NO with increasing O_2 fraction. In general, we can conclude that reasonable agreement is obtained be-

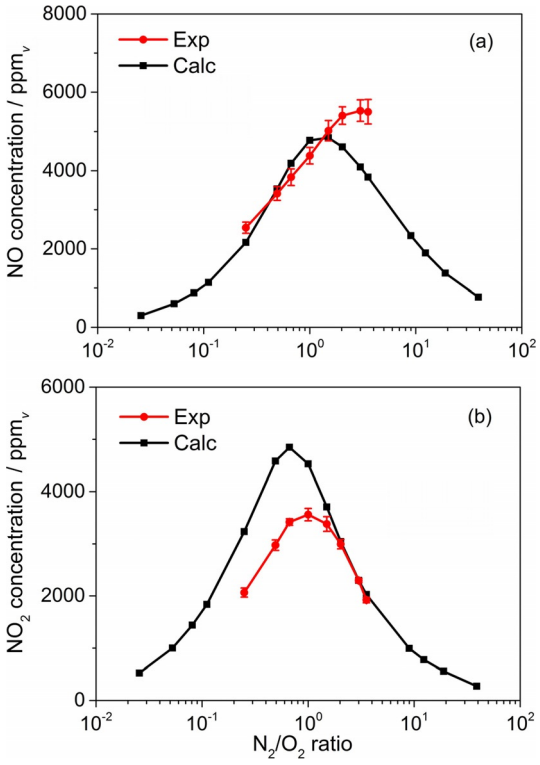

Figure 1. Experimental and calculated concentrations of NO (a) and NO_2 (b) as a function of the N_2/O_2 ratio in the feed gas, for a gas flow rate of 2 L min^{-1} and a SEI of 1.4 kJ L^{-1} (or 0.35 eV molec^{-1}).

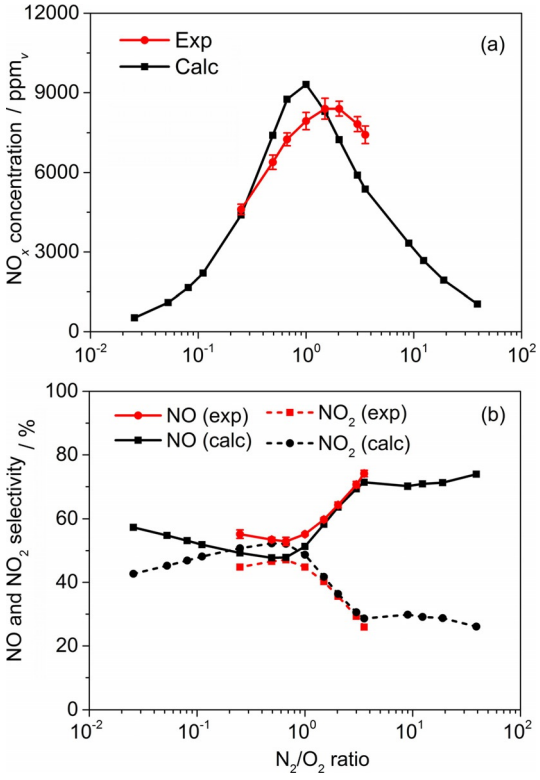

Figure 2. Experimental and calculated concentrations of NO_x (taken as $NO + NO_2$) (a) and NO and NO_2 selectivity (b) as a function of the N_2/O_2 ratio in the feed gas, for a gas flow rate of 2 L min^{-1} and a SEI of 1.4 kJ L^{-1} (or 0.35 eV molec^{-1}).

tween the experimental and calculated data, indicating that the model can provide a more or less realistic picture of the plasma chemistry, and can thus be used to elucidate the underlying mechanisms, as will be shown later.

Comparison of our results with thermal NO_x formation and with the H–B process

To evaluate the performance of our gliding arc for NF, we compare our results with the thermal NO_x yield, calculated as a function of gas temperature (see the calculation method in the Supporting Information). The NO_x yield calculated by the thermal model is based on the chemical equilibrium composition, which is calculated by finding the composition that minimises the Gibbs free energy. It is a standard technique in equilibrium chemistry and widely used in literature owing to the difficulties in performing experiments at such high temperature.[65,66]

Figure 3 shows the calculated equilibrium species composition of a 50% N_2/50% O_2 mixture, as a function of the gas temperature at atmospheric pressure. At room temperature, the thermal NO_x (i.e., $NO + NO_2$) yield is negligible because the species energy is not high enough to break the nitrogen bond. With increasing gas temperature, the molar fractions of NO and NO_2 increase. The selectivity of NO is higher than that of NO_2 owing to the dissociation of NO_2 into NO and O at higher temperature. The concentration of NO reaches a peak at around 3500 K. A further temperature increase yields a reduction of the NO yield, because of dissociation of NO into N and O atoms.

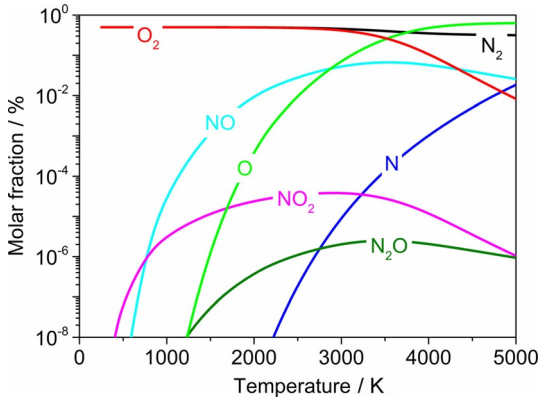

Figure 3. Calculated gas composition for a 50% N_2/50% O_2 mixture, as a function of the gas temperature at atmospheric pressure.

The variations in molar fractions of NO and NO_2 as a function of temperature explain why the thermal NO_x yield and corresponding energy efficiency both show a peak at a certain temperature, as illustrated in Figure 4. Our calculations predict the highest thermal NO_x yield of approximately 8% at 3500 K. The corresponding energy efficiency is then about 2.9%. At 3000 K, a somewhat higher energy efficiency of nearly 4% is reached, but the NO_x yield is then only 5.5%. The reason for reaching a higher energy efficiency at a somewhat lower temperature is

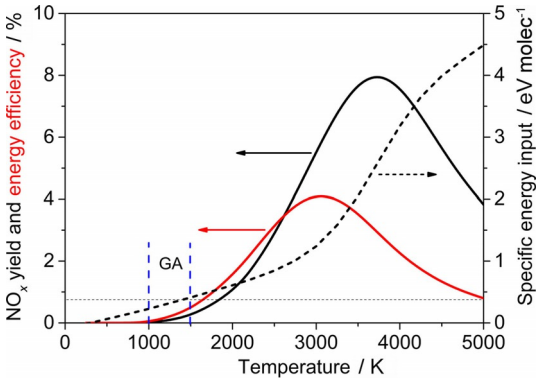

Figure 4. Calculated thermal NO_x yield (solid black line, left *y* axis) and corresponding energy efficiency (solid red line, left *y* axis), as well as the corresponding specific energy input (dashed line, right *y* axis), as a function of gas temperature for a 50% N_2/50% O_2 mixture at atmospheric pressure. The typical gas temperature range in our gliding arc (GA) is indicated with the blue vertical dashed lines.

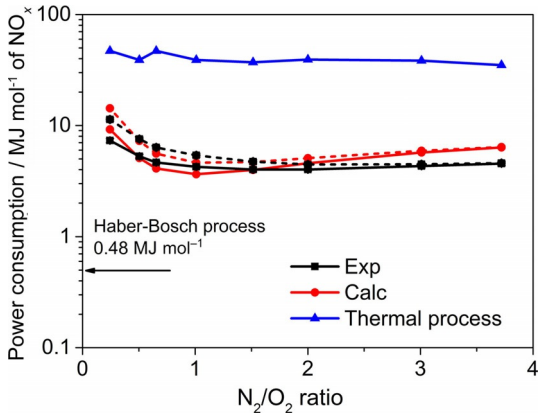

Figure 5. Experimental and calculated energy consumption of NO_x formation as a function of the N_2/O_2 ratio in the mixture, for a gas flow rate of 2 L min^{-1} and a SEI of 1.4 kJ L^{-1} (or 0.35 eV molec^{-1}), and comparison with the thermal process at the same SEI value. The solid and dashed (black and red) lines indicate without and with energy cost of air separation, respectively. The energy consumption of the H–B process is also presented for comparison.

simply because a lower specific energy input (SEI) is needed, as seen from the dashed curve in In Figure 4; we also indicate the typical gas temperature range in our gliding arc (see the blue vertical dashed lines). The thermal NO_x yield is only about 0.16% at 1500 K, which is the highest gas temperature in our gliding arc. Because only a limited fraction (around 7.8%; cf. Supporting Information) of the total gas flowing into the reactor during every gliding-arc cycle is processed by the effective gliding-arc volume (*v*), the thermal NO_x yield of 0.16% would correspond to an overall NO_x yield of only 25 ppm_v, which is a factor 320 lower than the value of nearly 8000 ppm_v that we measured in our gliding arc (cf. Figure 2a). Furthermore, if all the gas flowing into the reactor would be treated by the thermal process, an SEI of 1.4 kJ L^{-1} (or 0.35 eV molec^{-1}) would lead to an overall NO_x yield around 1095 ppm_v, which is still much lower than our measured value. This low NO_x concentration obtained by the thermal process demonstrates that most of the energy is spent on gas heating rather than on nitrogen oxidation, and that our gliding arc clearly operates in non-equilibrium conditions, explaining the much higher NO_x yield obtained compared to the thermal process.

The experimental and calculated energy consumption per mole of NO_x formed obtained with and without including the energy cost of gas preparation (i.e., air separation) is plotted in Figure 5 as a function of the N_2/O_2 ratio. At low N_2/O_2 ratios, only considering the plasma energy consumption, the energy required for NO_x formation slightly decreases with increasing N_2/O_2 ratio, up to a value of 37.1 MJ mol^{-1} at a N_2/O_2 ratio of 1, after which the experimental value remains constant, whereas the calculated value slightly increases again upon higher N_2/O_2 ratios. This is logical because the N_2/O_2 ratio around 1 gives rise to the highest calculated NO_x concentration. We have also included in Figure 5 the power consumption of NO_x formation, accounting for the energy cost of gas preparation (i.e., air separation), in case of a N_2/O_2 ratio different from air, and the results show a quite similar trend with variation of the N_2/O_2 ratio. The influence of the energy cost of gas preparation on the total energy consumption gradually decreases with increasing N_2 content. This is because the pure oxygen flow rate and hence the related energy cost of gas preparation decreases. With a feed ratio of 79% N_2/21% O_2, air as the only feed gas was found to produce a slightly lower amount of NO_x than the mixture with the optimised N_2/O_2 feed ratio of around 1.0, for which more energy is needed to prepare pure O_2 gas and this is definitely beneficial for the costs, yielding a lower total energy consumption, as indicated in Figure 5.

The current industrial-scale H–B process provides a benchmark for the energy consumption for plasma-based NF processes. The energy requirement for the H–B process is much lower, that is, 0.48 MJ mol^{-1} of N atoms.[67] This value includes the energy consumption during the whole industrial production process of ammonia using three main raw materials: natural gas, air and water. The current comparison indicates that plasma-based NF is not yet competitive with the industrial H–B process, which operates of course on a much larger scale. Hence, it is obvious that much more research is needed to further improve the plasma-based NF process. On the other hand, it is also clear from Figure 5 that the gliding arc requires about 10 times less energy than the thermal process of NO_x formation, calculated with the same energy input of 1.4 kJ L^{-1} (or 0.35 eV molec^{-1}). As the high temperature makes it very challenging to establish a thermal plasma in our gliding-arc reactor, it is difficult to validate our thermal conversion model by direct comparison under specific conditions. However, experimental work in the literature,[68–72] performed in other thermal plasma reactors to which our thermal conversion model is applicable, generally yield a higher energy consumption of NO_x synthesis than in our current work, because the energy in a thermal system is distributed over all degrees of freedom, including those not effective for the NO_x synthesis. This is in reasonable agreement with the prediction of our thermal model, although it is not really possible to compare different reactor setups with different discharge conditions.

The fact that the energy efficiency of the gliding arc for NO_x synthesis is much better than that for the thermal process can also be deduced from Figure 6. Indeed, both the calculated and measured energy efficiency, with and without considering the energy cost of gas preparation (i.e., air separation), are

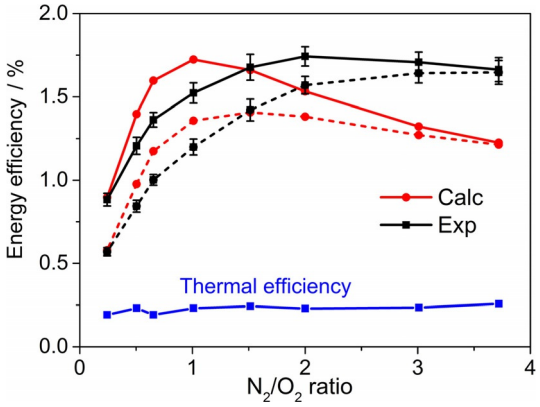

Figure 6. Experimental and calculated energy efficiency of NO_x formation as a function of the N_2/O_2 ratio in the mixture, for a gas flow rate of 2 L min^{-1} and a SEI of 1.4 kJ L^{-1} (or 0.35 eV molec^{-1}), and comparison with the thermal energy efficiency at the same SEI value. The solid and dashed (black and red) lines indicate without and with the energy cost of air separation, respectively.

around 0.5–1.7%, whereas the thermal energy efficiency calculated for the same SEI of 1.4 kJ L^{-1} is only about 0.2%. Hence, this clearly demonstrates the non-equilibrium character of the gliding arc for NO_x synthesis, that is, the NO_x synthesis does not proceed thermally but upon electron-induced processes, contributing to energy efficient chemical reactions, as will be explained below. Moreover, when including the energy cost related to the gas preparation (i.e., producing pure O_2 gas from air), the experimental energy efficiency using air (i.e., N_2/O_2 ratio of 79%:21%) shows the highest value of all different feed ratios, although the addition of oxygen to air slightly enhances the production of NO_x to some extent. This once again shows that inexpensive and readily available atmospheric pressure air is suited and preferred instead of an artificial N_2+O_2 mixture.

Underlying mechanisms of NO_x formation in the gliding arc: energy efficient process by vibrational excitation of N_2

As mentioned above, the NO_x formation in our gliding arc, as well as in other types of plasmas, is induced by electron impact reactions with the N_2 and O_2 molecules. In Figure 7, we illustrate how the electron energy is transferred to different channels of excitation, ionization and dissociation of both N_2 and O_2 molecules in a 50% N_2/50% O_2 mixture, as a function of the reduced electric field (*E*/*N*, where *E* is electric field and *N* is concentration of neutral particles) in the discharge. This reduced electric field is an important parameter to distinguish different plasma types, as it determines the average electron energy in the plasma, and thus the rate of the various electron impact reactions. The electron energy values corresponding to

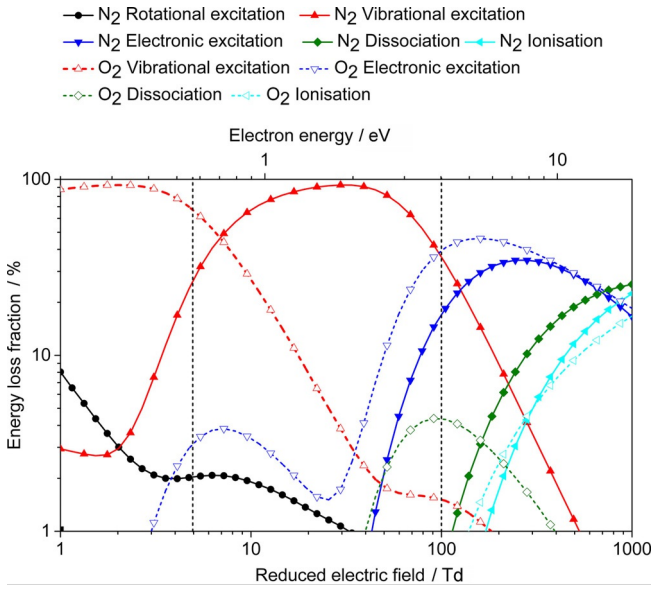

Figure 7. Fraction of electron energy transferred to different channels of excitation, as well as ionization and dissociation of N_2 and O_2, in a 50% N_2/50% O_2 mixture, as a function of the reduced electric field (*E*/*N*), as calculated from the corresponding cross sections of the electron impact reactions. The reactions with N_2 are indicated with solid lines, whereas the corresponding reactions with O_2 are plotted with dashed lines. The electron energies corresponding to the reduced electric field values are indicated at the top *x* axis. The region between the two dashed vertical lines, indicating a reduced electric field between 5 and 100 Td, corresponds to the typical gliding-arc regime.

the reduced electric field values are thus also indicated in Figure 7 (see top and bottom *x* axes). A gliding arc is typically characterised by reduced electric field values between 5 and 100 Td (see the vertical dashed lines in Figure 7), whereas a dielectric barrier discharge (DBD), which is a quite popular type of plasma for gas conversion applications, typically operates at values higher than 100 Td.[31] Note that 1 Td (Townsend) corresponds to 10^{-21} V m^{-2}.

It is known that the energy efficiency of NO_x formation is determined by the method to break the strong ($\approx$10 eV) bond of the N_2 molecule. Above approximately 100 Td, as we can see from Figure 7, most electron energy goes into electronic excitation, dissociation and ionisation of the N_2 (and O_2) molecules. The N atoms produced by direct electron impact dissociation of N_2 molecules can react with O_2 molecules to form NO. However, owing to the very high dissociation threshold level of N_2, the energy efficiency in this case would be limited to a low level of about 3%.[31] This explains why a DBD is characterised by a lower energy efficiency, or a higher energy consumption for NO_x synthesis. Indeed, in Ref. [73], an energy consumption of 18.0 MJ mol^{-1} was obtained for NO_x synthesis in a DBD reactor, which is clearly lower than in our case. We can describe this mechanism as follows in Equations (1) and (2):

$$e^- + N_2 \rightarrow N_2(a^1\Pi_g),\ N_2(B^3\Pi_g),\ N_2(b^1\Pi_u) \\ +e^- \rightarrow e^- + N + N \quad (1)$$

$$N + O_2 \rightarrow NO + O,\ E_a \approx 0.3\,eV\,molec^{-1}$$
$$\Delta H \approx -0.94\,eV\,molec^{-1} \quad (2)$$

A similar mechanism, based on electron impact dissociation of N_2, was also predicted by our model, and validated by experiments, for a CO_2/N_2 mixture in a DBD reactor.[50]

On the other hand, in the reduced electric field range lower than 100 Td, which is characteristic for our gliding arc, electron impact vibrational excitation of N_2 is the dominant electron process, as is clear from Figure 7, and the resulting N_2 molecules in vibrational levels will be important for NO formation in our case. Indeed, the relatively high energy barrier of the reaction between N_2 molecules and O atoms to form NO, that is, approximately 3 eV, can be overcome by the vibrational energy of the N_2 molecules. As a result, the so-called Zeldovich mechanism stimulated by vibrational excitation [31] will play the dominant role for producing NO in our gliding arc, whereas the N formed in this process can react with an O_2 molecule to form another NO [Eqs. (3), (4)]:

$$O + N_2(v) \rightarrow NO + N,\ E_a \approx \Delta H \approx 3\,eV\,molec^{-1} \quad (3)$$

$$N + O_2 \rightarrow NO + O,\ E_a \approx 0.3\,eV\,molec^{-1}$$
$$\Delta H \approx -0.94\,eV\,molec^{-1} \quad (4)$$

(v) indicates in vibrational state. This will be further elaborated in the next section.

To demonstrate that the N_2 vibrational levels are indeed important in our gliding arc, we plot in Figure 8 the vibrational distribution of N_2 in the gliding arc at four different times, that is, at 5 μs (corresponding to the beginning of the first pulse; see the Supporting Information for details), 15, 25, and 35 μs (i.e., at the end of the first pulse). At the time instant of 5 μs, mainly the low vibrational levels are populated, owing to electron excitation. When time evolves, the fast vibrational–vibrational (VV) relaxation, which represents the vibrational energy exchange among two molecules in the same mode of vibration, leads to the establishment of a vibrational distribution in which the high-energy levels are also gradually more populated, as is clear from Figure 8. If the vibrational energy lost to translational degrees of freedom (i.e., vibrational–translational (VT) relaxation processes) and chemical reactions would be neglected, the vibrational levels would show a Treanor distribution, that is, an exponentially parabolic distribution function with a minimum value at intermediate vibrational levels.[74] However, when the chemical reactions of the vibrational levels are taken into account, the highest vibrational levels can overcome the reaction energy barrier. As a result, the destruction rate of the high vibrational levels is very large and the normalised vibrational distribution function shows a decreasing trend with a larger slope with rising vibrational levels. By comparing the vibrational distribution functions calculated in the gliding arc with the equilibrium thermal distribution, calculated for a gas temperature of 1500 K, which is also plotted in Figure 8, it is obvious that the gliding arc discharge is highly vibrationally overpopulated throughout the entire power deposition pulse (or discharge cycle), explaining the important role of the N_2 vibrational levels in the NO formation in our gliding arc (see also next section).

Figure 9 illustrates the calculated vibrational temperature of N_2 as a function of time during the entire gliding-arc discharge stage. It is defined as follows from the first vibrational level [Eq. (5)]:

$$T_v = \frac{E_{v1}}{k_B \ln(n_1/n_0)} \quad (5)$$

where the v stands for vibrational state $E_{v11}/k_B = 3481$ K is the energy of N_2(v1) and n_1 and n_0 are the densities of N_2(v1) and N_2 ground state, respectively. k_B is the Boltzmann constant.

In our experiments, we use a high-frequency pulsed power, which leads to oscillations in the power deposition. Therefore, the electron temperature and electron number density also show this oscillation behaviour (see details in the Supporting Information). Hence, it is clear that the vibrational temperature, which is determined by electron impact vibrational excitation, and thus strongly depends on the electron properties (see de-

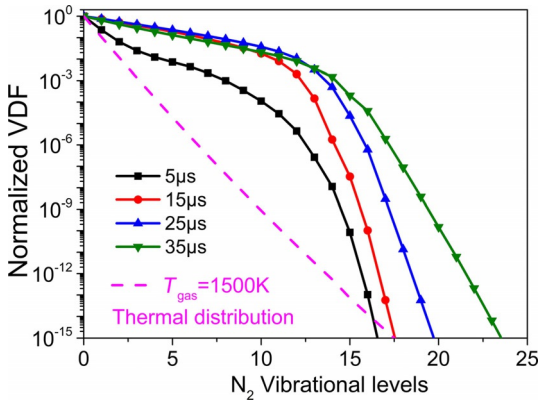

Figure 8. Normalised vibrational distribution function at different time instants of the first discharge pulse for a 50% N_2/50% O_2 mixture. The thermal distribution at the gas temperature of 1500 K is also presented for comparison.

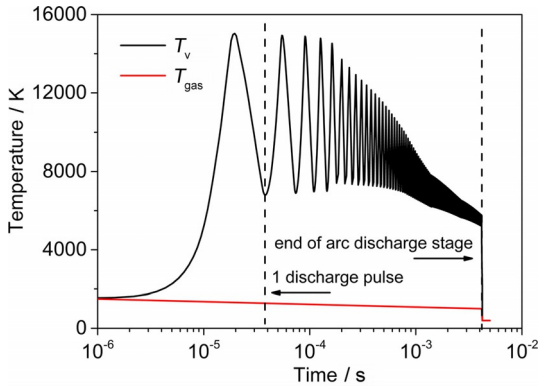

Figure 9. Vibrational temperature of the first vibrational (T_v) state of N_2 as a function of time in the gliding arc discharge for a 50% N_2/50% O_2 mixture. The gas temperature is also presented for comparison.

tails in the Supporting Information), also exhibits the same oscillations, with a peak at maximum power deposition of one discharge pulse, which drops again with the decrease of the power deposition. However, when the power drops to zero, the vibrational temperature is still higher than the gas temperature because it cannot relax back to the gas temperature in the limited timescale before the start of the next power deposition pulse, when the vibrational temperature rises again. The maximum vibrational temperature, however, decreases with time because both the power density and electron number density decrease (see Figure S5 in the Supporting Information), and the electron energy transfer to vibrational energy by electron impact vibrational excitation is thus reduced. Near the end of the arc discharge stage, the vibrational temperature does not show a large variation during and in between two discharge pulses, but the it is still considerably higher than the gas temperature (i.e., about 5000 vs. 1000 K), indicating that the vibrational levels are overpopulated during the entire gliding arc cycle, and thus that the gliding arc is far from thermal equilibrium. Our calculated values of the vibrational temperature range from 4500 to 8000 K, which is in general good agreement with experimental investigations[75,76] for a kHz alternating current (AC) air gliding arc at atmospheric pressure.

It should be noted that not only the N_2 molecules but also the O_2 molecules are vibrationally excited in the gliding arc. The latter can also help overcome the reaction energy barrier of the NO formation process (see [Eq. (4)] above). However, as we can see from Figure 7, the electron energy is more easily transferred to the vibrational energy of the N_2 molecules in the typical reduced electric field range of a gliding arc. Therefore, we only present here the results of the N_2 vibrational levels. In the next section we will try to elucidate the role of the various plasma chemical reactions and plasma species, and especially of the vibrational levels, on the actual NO_x synthesis in our gliding-arc reactor.

Formation and loss processes of NO and NO_2

To better understand the influence of the N_2/O_2 feed ratio on the NO_x yield, we investigated the dominant reaction pathways for the formation and loss of NO and NO_2 for several N_2/O_2 feed ratios. This kinetic analysis was performed by looking at the time and volume integrated rates of the various processes for the total residence time of 5.0 ms (cf. Figure S3 in the Supporting Information).

Table 1 lists the most important formation (F1–F6) and loss (L1–L5) processes for NO. In the Supporting Information (Figure S6) we plot their time and volume integrated rates as a function of N_2/O_2 ratio, as well as the total formation and loss rate. As explained in the Supporting Information, some formation reactions are counteracted by some loss reactions. Hence, to investigate the net contribution of the forward and reverse reactions to the formation of NO, we plot in Figure 10 the time and volume integrated net rates of the various NO formation processes as a function of N_2/O_2 ratio, as well as the total net formation rate.

Table 1. Overview of the most important formation and loss reactions for NO.

Formation processes		Loss processes	
F1	$O+N_2(v)\rightarrow NO+N$	L1	$N+NO\rightarrow O+N_2$
F2	$O+NO_2\rightarrow NO+O_2$	L2	$O+NO\rightarrow NO_2$
F3	$N+O_2/O_2(v)\rightarrow NO+O$	L3	$NO+NO_2+M\rightarrow N_2O_3+M$
F4	$N_2O_3+M\rightarrow NO+NO_2+M$	L4	$NO_3+NO\rightarrow NO_2+NO_2$
F5	$N+NO_2\rightarrow NO+NO$	L5	$NO_2^-+NO_2\rightarrow NO_3^-+NO$
F6	$NO_2^-+NO_2\rightarrow NO_3^-+NO$		

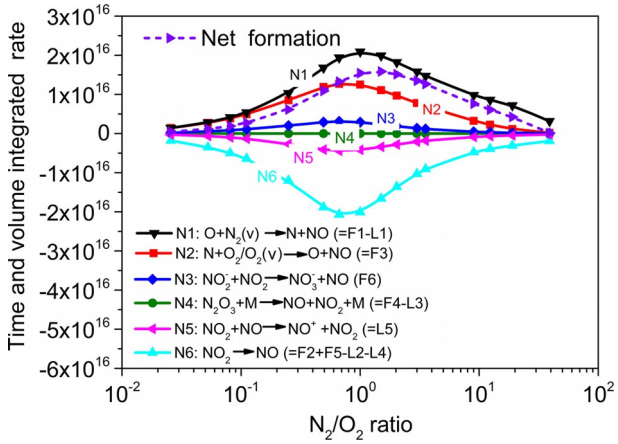

Figure 10. Time and volume integrated net rates of the various NO formation processes as a function of N_2/O_2 ratio, for a SEI of 1.4 kJ L^{-1} (or 0.35 eV $molec^{-1}$), as well as the total net formation rate.

Although the collision between oxygen atoms and NO_2 (F2 in Table 1) is the dominant formation mechanism of NO at low N_2/O_2 ratio, or high oxygen contents in the mixture, as shown in Figure S6, the reactions that proceed from NO_2 have an overall negative net contribution to the NO formation, as is obvious from Figure 10 (see N6). This indicates that there is more formation of NO_2 from NO than vice versa, and reaction F2 does not count as net formation process of NO. In contrast, the rate of reaction F1 is 18% higher than the rate of its reverse reaction L1 at the N_2/O_2 feed ratio of 1.0 (see Figure S6), and thus, reaction F1 has a clear net contribution to NO formation (see N1 in Figure 10). From this analysis we can therefore draw the following conclusion: the Zeldovich mechanism stimulated by vibrational excitation (F1 in Table 1) is the dominant production process of NO in the gliding arc, but the NO synthesis could be further enhanced if its reverse reaction (L1) could be reduced. Additionally, the second important formation process of NO is the reaction of N atoms with O_2 molecules (either in ground state or vibrational levels) (F3), so we should aim to steer the N atoms, formed in reaction F1, to react with O_2 molecules in reaction F3, instead of reacting with the NO molecules in the reverse reaction L1, to optimise the NO synthesis.

Table 2 lists the most important formation (F7–F10) and loss (L6–L11) processes for NO_2. Their time integrated rates are plotted in Figure S7 in the Supporting Information, as a function of N_2/O_2 ratio, as well as the total formation and loss rate.

Table 2. Overview of the most important formation and loss reactions for NO_2.

Formation processes		Loss processes	
F7	$O+NO \rightarrow NO_2$	L6	$O+NO_2 \rightarrow NO+O_2$
F8	$N_2O_4+M \rightarrow NO_2+NO_2+M$	L7	$NO_2+NO_2+M \rightarrow N_2O_4+M$
F9	$NO_3+NO \rightarrow NO_2+NO_2$	L8	$NO_2+NO_2 \rightarrow NO_3+NO$
F10	$N_2O_3+M \rightarrow NO+NO_2+M$	L9	$NO+NO_2+M \rightarrow N_2O_3+M$
		L10	$N+NO_2 \rightarrow NO+NO$
		L11	$N+NO_2 \rightarrow O+N_2O$

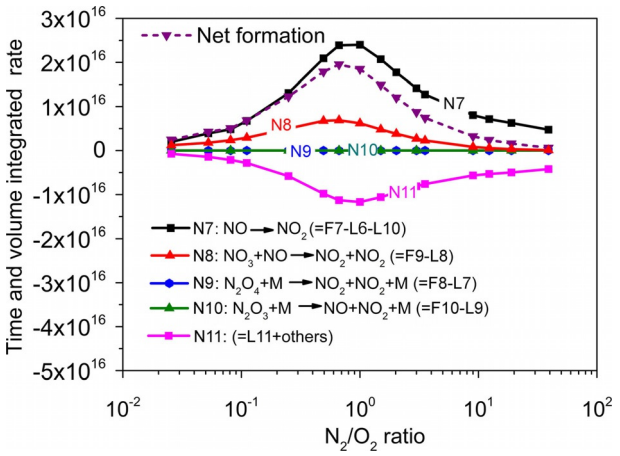

Figure 11. Time and volume integrated net rates of various NO_2 formation processes as a function of N_2/O_2 ratio, for a SEI of 1.4 kJ L^{-1} (or 0.35 eV molec^{-1}), as well as the total net formation rate.

Figure 11 shows the time and volume integrated net rates of the various NO_2 formation processes as a function of N_2/O_2 ratio. Although the reactions involving N_2O_4, that is, F8 and L7, are the dominant formation and loss mechanism of NO_2 at N_2/O_2 feed ratio between 0.2 and 10, as shown in Figure S7 in the Supporting Information, their absolute reaction rates are nearly balanced. Therefore, these reactions (combined as N9) have a negligible net contribution to the formation of NO_2. The same applies to the reaction N10, involving N_2O_3 (F10 and L9). Our calculations clearly indicate that the oxidation of NO via F7 is the most important net formation process of NO_2 (N7).

Overall reaction scheme of the NO_x chemistry

The data revealed by our 0D model allow us to compose an overall reaction scheme for the NO_x synthesis, as depicted schematically in Figure 12. The 9.8 eV strong triple bond of N_2 is mainly broken by vibrational excitation, followed by the reaction of N_2(v) with O atoms into NO and N [Eq. (3)]. The N atoms subsequently react with O_2 molecules to form a second NO and a new O atom [Eq. (4)]. The reaction chain is closed when the new O atom reacts with the next vibrationally excited N_2 molecule. Overall, NO is thus mainly produced by the non-thermal Zeldovich mechanism stimulated by vibrational excitation in the gliding arc. Indeed, the average electron energy in the gliding arc is in the range of 0.6–4.0 eV, which results in about 50–90% electron energy transfer to N_2 vibrational excitation (see Figure 7), whereas VV relaxation further populates the higher N_2 vibrational levels. The latter helps overcome the high reaction energy barrier of the Zeldovich reaction (3 eV molec^{-1}) and to promote the production of NO. Therefore, it is crucial to tune the reduced electric field (*E*/*N*) in the gliding arc to establish an energy-efficient way of NO production by the non-equilibrium plasma.

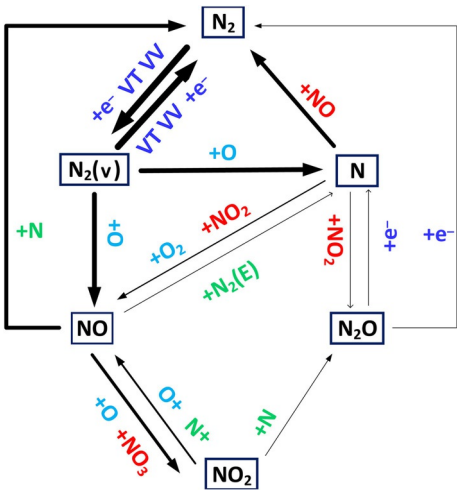

Figure 12. Reaction scheme to illustrate the main pathways of the NO_x chemistry in the gliding arc as predicted by our model. The thickness of the arrows corresponds to the importance of the reactions for a 50% N_2/50% O_2 mixture. For instance, the thickness of the arrow from N_2(v) to NO corresponds to a time and volume integrated rate of 1.37×10^{17}. N_2(E) indicates the sum of all the electronically excited N_2 molecules.

Our simulations indicate that for a total gliding arc cycle, a local NO_x concentration as high as 20% can be reached within the gliding-arc volume. A large fraction of the produced NO is, however, readily destroyed upon impact with N atoms in the active plasma zone (see also Figure 12). By artificially setting the reaction rate of reaction L1 (Table 1) to zero, our model calculations predict a much higher NO yield of 24588 ppm_v for a N_2/O_2 feed ratio of 1, which is around 5 times the yield obtained in Figure 1, by taking into account this loss reaction. Consequently, the energy efficiency will also increase by a factor around 5. This clearly shows that suppressing the loss processes of reaction L1 will enhance the NO_x yield and hence the overall energy efficiency. The reverse reaction L1 indeed competes with the propagation (reaction F3 in Table 1) of the Zeldovich chain, and it is able to terminate the chain when the NO concentration becomes high in the active discharge zone. This seriously restricts the yield of NO synthesis in our gliding arc. As a result, we should look for ways of suppressing the reverse reaction L1 or promoting the reaction F3, to increase the NO yield and hence improve the energy efficiency. For example, at a fixed SEI, by increasing the gas flow rate, the gas velocity becomes larger than the arc velocity and a larger amount of feed gas will be exposed to the plasma. The local NO concentration inside the arc would then decrease, but the overall NO yield and hence the energy efficiency would rise. Our experimental results for the NO_x con-

centration versus SEI indeed show that higher flow rates can produce higher NO_x concentrations at a fixed SEI. This shows the high potential of the gliding arc discharge for NO_x production at higher flow rates.

The promotion of the reaction F3 can be reached when making use of hot N atoms. Indeed, the vibrational energy of $N_2(v)$ is higher than the activation energy of the reaction F1 (i.e., 3.0 eV) for vibrational levels above v12, which corresponds to a vibrational energy of 3.2 eV. Thus, a fraction of the vibrational energy released goes into translational energy of the N atoms (so-called hot N atoms) and assists in the reaction F3, by increasing the rate coefficient of this reaction, and therefore, the NO yield can be enhanced. It is shown in Ref. [77] that increasing the oxygen content in the mixture can help to enhance this effect and promote the reaction F3.

Our reaction scheme (Figure 12) also shows that NO_2 is mainly formed by oxidation of NO upon reaction with O atoms, whereas it mainly reacts back into NO upon reaction with either O or N atoms, at high or low oxygen contents, respectively. The main channel responsible for the formation of O atoms, which are important to initiate the Zeldovich mechanism via reaction F3, is electron-impact dissociation of O_2 molecules.

Because the N atoms are lost rapidly via reaction L1, as well as by reactions with NO_2, our calculations indicate that the overall N concentration is never more than 0.1%. For this reason, N_2O, which is mainly produced upon reaction between N atoms and NO_2 (reaction L11 in Table 2), has only a minor concentration in the whole gliding-arc cycle compared with NO and NO_2. This is in qualitative agreement with our experiments, as no N_2O was detected.

As mentioned above, the industrial scale H–B process still has a lower energy consumption, that is, 0.48 MJ mol^{-1} N, so it is clear that major efforts should be taken in gliding arc plasma-based NF to further increase the yield and decrease the energy consumption, to become competitive with the industrial scale H–B process. Computer simulations, as presented here, can help to improve the process, as they elucidate the limiting factors for energy-efficient NO_x synthesis, and thus can help provide solutions to overcome these limitations.

On the other hand, it is important to realise that more and more electrical energy nowadays is produced from renewable energy sources (wind or solar), and this trend will continue in the coming years. As renewable energy sources often suffer from fluctuating peak powers (e.g., on windy or sunny days) when the electricity is in principle "for free", our high-frequency pulsed gliding arc plasma can be very useful for peak shaving, as it is very flexible and can be switched on and off easily, so we expect that it will be very suitable for NF by NO_x synthesis using renewable energy. Furthermore, as an instantaneous "on-and-off" technique, the gliding-arc-based NF can be stopped and started more easily than the H–B process, making it possible for farmers in remote locations to locally generate the necessary nitrogenous fertilisers out of "thin air" just using small-scale plants. This application of gliding-arc technology is very promising, especially in regions where a wealth of underused wind and solar resources exist, which offer farmers a new source of revenue from their land—a renewable alternative to conventional nitrogenous fertilisers that is compatible with growing crops because of its high operation flexibility.

Conclusions

The purpose of this work was to obtain a better understanding of the nitrogen fixation (NF) process through NO_x synthesis in gliding arc plasma, by means of combined experiments and a zero-dimensional kinetics model. We compared our experimental data with the model predictions and obtained reasonable agreement for the NO, NO_2, and total NO_x yield, the NO and NO_2 selectivity, the energy consumption and energy efficiency for the entire range of N_2/O_2 feed ratios in the mixture. This indicates that our model can provide a realistic picture of the plasma chemistry and can be used to elucidate the dominant reaction pathways for the NO_x synthesis.

Our study clearly reveals that vibrational excitation of N_2 can help overcome the reaction energy barrier of the non-thermal Zeldovich mechanism: $O + N_2(v) \rightarrow NO + N$, and can thus significantly enhance the production of NO. This provides an energy efficient pathway for NO formation in the gliding arc. Furthermore, our simulation shows that the most important reaction for NO_2 formation is oxidation of NO by O atoms: $O + NO \rightarrow NO_2$.

We also compared our results with those of thermal NO_x synthesis. The NO_x yield and energy efficiency obtained in our gliding arc are much higher than the thermal values owing to the non-equilibrium properties of the plasma, as the chemistry of the conversion process is induced by energetic electrons. We can conclude that the gliding arc is a very promising candidate for potential industrial scale NF, but the energy consumption achieved in this study is still much higher than the benchmark, that is, the industrial Haber–Bosch process. Therefore, it is clear that the NO_x synthesis in the gliding arc should be further improved, for example, by operating at conditions in which the reverse reaction $N + NO \rightarrow O + N_2$ is suppressed or where the reaction $N + O_2/O_2(v) \rightarrow NO + O$ is promoted, as our simulations indicate that these processes currently limit the NO_x formation.

In general our model allows us to gain better insights into the entire process of NO_x formation, which enables us to propose solutions for improving the gliding-arc-based NO_x synthesis processes in the future. One example could be to actively tune the reduced electric field (i.e., *E/N* ratio) by optimizing the reactor electrical operational parameters, to promote the vibrational excitation and selectively deliver energy to the Zeldovich chemical reaction of NO synthesis by an energy efficient way. Another example could be to improve the reactor geometry and optimise the flow conditions to expose the maximum amount of feed gas to the gliding arc.

It is clear that NF in the gliding arc is still far from competitive with the world-scale business case of the Haber–Bosch process, but if electricity from sustainable energy sources can be used, the intrinsic potential of gliding-arc-based NF can provide a promising opportunity of producing fertiliser in remote locations. This comes up with realistic scenarios of en-

tering a cutting-edge innovation in new business cases of plasma agriculture.

Furthermore, for practical applications, it would be beneficial to make use of air, which includes a certain amount of humidity. Electric discharges in humid air have been studied already in literature; they produce more reactive species and present highly acid and oxidizing properties towards aqueous solutes.[78] These chemical effects can be used for various practical applications, for example, the removal of major pollutants from waste waters.[79] However, the interaction mechanism of water vapour with air (N_2/O_2) is not yet precisely clarified. Our current work shows that the NO_x formation by the gliding arc operating in dehumidified air strongly depends on the composition of the feed gas, in which the nature of the interactions, such as vibrational molecular excitation between the constituents, is very important. Therefore, identifying the role of different species, and especially their excited states, and clarifying the underlying chemistry in humid air, for different degrees of humidity, will be of great interest to investigate how to enhance nitrate formation in a humid air gliding arc. This is planned for our future work.

Experimental Section

Experimental studies

The experiments were performed at atmospheric pressure in a milli-scale gliding-arc reactor. This is a two-dimensional flat reactor in which the gas flow enters through a nozzle at the bottom of the reactor (see Figure 13a). The reactor consists of two thin diverging knife-shaped molybdenum electrodes with thickness of 1.0 mm and height of 195 mm. The width of the reactor is 135 mm with narrowest discharge gap of 1.3 mm. A schematic diagram of the experimental set-up with milli-scale gliding-arc reactor is also shown in Figure 13b. One of the electrodes is connected to the high-voltage source and the other electrode is grounded. The reactor is powered by a customised Xenionik EP 4000 AC power supply. The applied high voltage and current were measured by a high voltage probe (Tektronix P6015A) and a current sense resistor of 5 Ω, respectively. All electrical signals were recorded using a USB powered four-channel PC oscilloscope (PicoScope R 3000).

Air and O_2 (Linde Gas, 99.9%) were fed into the reactor using mass flow controllers (Bronkhorst) and no pre-heating of the gas occurred. The products were analysed using a Fourier Transform Infrared Spectrophotometer (SHIMADZU, IRTracer-100) at a resolution of 0.5 cm^{-1} and the gas cell was equipped with CaF_2 windows (Specac, Storm Series). NO and NO_2 were the only products detected and their concentrations were determined from the adsorption bands at 1900 and 1630 cm^{-1}, respectively, using a series of calibration gas mixtures. The reported NO and NO_2 selectivity was calculated using Equations (6) and (7):

$$\text{NO selectivity} = \frac{\text{NO concentration}}{\text{concentration of } (NO + NO_2)} \quad (6)$$

$$NO_2 \text{ selectivity} = \frac{NO_2 \text{ concentration}}{\text{concentration of } (NO + NO_2)} \quad (7)$$

The arc dynamics in the plasma reactor was obtained using high-speed imaging. This helped us to compute the gliding arc lifetime, velocity, propagation height and processing time, all of which were used as input in the model (see the Supporting Information). The performance of the milli-scale gliding-arc reactor was investigated at a constant flow rate of 2 L min^{-1}, pulse width (25 μs) and amplitude (70 Vpk-pk (peak-to-peak voltage)), and by varying the feed ratio of Air/O_2, yielding N_2/O_2 ratios of 0.25–4. All experiments were performed four times and averages of at least 100 voltage–current (*V–I*) cycles were used to obtain the final power consumption value. The experiments were reproducible within +/− 5% of the averaged values. The error bars in Figures 1, 2, 5 and 6 show the 95% confidence interval. The influence of different flow rates, pulse widths and amplitudes on the NO_x yields was investigated in previous work[37] and is beyond the scope of our current work. We tested that Air + O_2 and N_2 + O_2 feed gas mixtures with the same ratio of N_2/O_2 gave very similar concentrations of NO_x as well as selectivity towards NO, indicating that the minor components in air, such as argon and carbon dioxide, have limited influence on the NO_x (i.e., NO + NO_2) yield.[80] Therefore, for simplicity, we assumed the air is composed of N_2/O_2 = 79:21 in our simulation mentioned below.

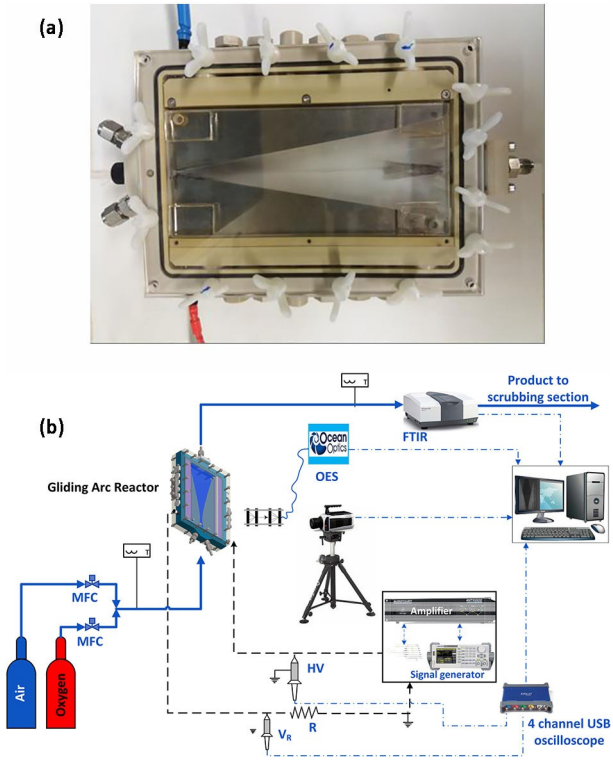

Figure 13. Reactor geometry (a) and schematic diagram of the experimental setup (b).

The total plasma power (P_{plasma}), specific energy input (SEI), and energy consumption (EC) per mole of NO_x are defined by Equations (8)–(10), respectively (GA: gliding arc).

$$P_{plasma}(W) = f \int_0^{t=t_{pulse}} V_{GA} \times I_{GA} dt \quad (8)$$

$$SEI\ [J\,L^{-1}] = \frac{P_{plasma} \times 60\ [s\ min^{-1}]}{\text{gas feed flow rate } [L\ min^{-1}]} \quad (9)$$

$$EC\ [J\,mol^{-1}] = \frac{P_{plasma} + P_{gp}}{\text{moles of } NO_x \text{ produced per second}} \quad (10)$$

where t_{pulse} is the time span of a pulse (s) and f is the frequency of the pulses (Hz). P_{gp} (W) is the power consumption used to prepare pure oxygen gas from the air by separation [Eq. (11)]:

$$P_{gp} = \frac{O_2 \text{ flow rate } [L\,min^{-1}] \times O_2 \text{ specific power to separate air } [W\,L^{-1}]}{60\,[s\,min^{-1}]} \quad (11)$$

where oxygen specific power for air separation is the power needed to produce a standard litre oxygen gas; a value of 0.28 $kW\,L^{-1}$ is used here, based on Ref. [81].
Likewise, the energy efficiency, η, is calculated as [Eq. (12)]:

$$\eta[\%] = \frac{H_{NO_x} \times \text{moles of } NO_x \text{ produced per second}}{P_{plasma} + P_{gp}} \quad (12)$$

where H_{NO_x} [$J\,mol^{-1}$] is the standard formation enthalpy of 1 mol NO_x, which is evaluated by Equation (13):

$$H_{NO_x} = H_{NO} \times S_{NO} + H_{NO_2} \times S_{NO_2} \quad (13)$$

Where H_{NO} and H_{NO_2} is the standard formation enthalpy of 1 mol NO (90.3 $kJ\,mol^{-1}$) and NO_2 (33.1 $kJ\,mol^{-1}$), respectively, and S_{NO} and S_{NO_2} is the selectivity of formed NO and NO_2 in the NO_x products.

Computational studies

0D chemical kinetics model

To elucidate the underlying mechanisms of the gliding arc assisted NO_x synthesis in the above-mentioned experimental setup, we developed a 0D plasma chemistry model, which allows to describe the behavior of a large number of species, and incorporate a large number of chemical reactions, with limited computational effort.
The zero-dimensional (0D) chemical kinetics model is based on solving balance equations for all the species densities, based on production and loss rates, as defined by the chemical reactions:

$$\frac{dn_i}{dt} = \sum_j \left\{ \left(a_{ij}^{(2)} - a_{ij}^{(1)} \right) k_j \prod_l n_l^{a_{ij}^{(1)}} \right\} \quad (14)$$

Where $a_{ij}^{(1)}$ and $a_{ij}^{(2)}$ are the stoichiometric coefficients of species i, at the left and right hand side of a reaction j, respectively, n_l is the species density at the left-hand side of the reaction, and k_j is the rate coefficient of reaction j. Transport processes such as diffusion are not considered; hence, the species densities are assumed to be constant in the entire simulation volume but they change with time. Nevertheless, this 0D model allows to describe the spatial dependence of the NO_x synthesis in the gliding-arc reactor, as explained in the Supporting Information.
The solution of the ordinary differential [Eq. (14)] for the various plasma species is coupled with the Boltzmann equation, which is solved for the electron energy distribution function (EEDF). We use an existing code ZDPlasKin,[82] which features an interface for the description of the plasma species and reactions, a solver for the set of differential [Eq. (14)], and an integrated Boltzmann equation solver BOLSIG+.[83]

Plasma chemistry included in the model

The species taken into account in our model for the N_2/O_2 mixture are listed in Table 3. These species include various neutral molecules in the ground state, as well as several electronically and vibrationally excited levels, various radicals, positive and negative ions, and the electrons.
We pay special attention to the electronically and vibrationally excited states of N_2 and O_2, because they may become important under certain conditions. The detailed notations of the N_2 electronically excited levels are given in the table, while the vibrational levels of both N_2 and O_2 are indicated with (v). 15 vibrational levels are taken into account for O_2, while for N_2, 25 vibrationally excited levels are included. The populations of the higher levels are negligible, as was demonstrated in Figure 8.
All these species undergo a large number of chemical reactions, that is, electron impact collisions with neutral species, leading to excitation, ionization, dissociation and electron attachment, electron-ion recombination reactions, as well as many heavy-particle chemical reactions (i.e., ion–ion, ion–neutral and neutral–neutral reactions).
The chemistry set used in this model is mostly based on the models recently developed within our group, and validated for a microwave discharge[49] and a DBD discharge[50] in a CO_2/N_2 mixture. The corresponding rate coefficients, and the references where these data were adopted from, are listed in the Supporting Information of the previous work.[49] Some adjustments to the major neutral reactions involving NO_x were made and their corresponding rate constants are listed in Table 4. The first and fifth reaction do not only apply to N_2 and O_2 molecules in the ground state, respectively, but also to vibrational levels, with the rate coefficients adapted, as elaborated in the supporting information.
Because the vibrational energy can help overcome the activation energy barrier of the reaction and thus increase the reaction rate constant, we present in the supporting information in detail the reactions of the vibrational levels, that is, electron impact excitation, vibrational energy exchange (VT and VV relaxation) reactions and chemical reactions (see section 1: Treatment of the vibrational level in the Supporting Information).

Table 3. List of species included in the model for the N_2/O_2 gas mixture.

Ground neutral species	Charged species	Excited species
N_2, N	N^+, N_2^+, N_3^+, N_4^+	$N_2(A^3\Sigma_u^+)$, $N_2(B^3\Pi_g)$,$N_2(W^3\Delta_u)$, $N_2(B'^3\Sigma_u^-)$, $N_2(C^3\Pi_u)$, $N_2(E^3\Sigma_g^+)$, $N_2(a'^1\Sigma_u^-)$, $N_2(a^1\Pi_g)$, $N_2(a''^1\Sigma_g^+)$, $N_2(w^1\Delta_u)$, N_2(V1-V25), N(2D), N(2P)
O_2, O_3, O N_2O, N_2O_4, N_2O_5, NO,NO_2, NO_3	O^+, O_2^+, O_4^+, O^-, O_2^-, O_3^-, O_4^- NO^+, N_2O^+, NO_2^+, NO^-, N_2O^-, NO_2^-, NO_3, $O_2^+N_2$ electrons (e^-)	O_2(V1-V15), O_2(E1)[a], O_2(E2)[b]

[a] O_2(E1) = sum of the $A^1\Delta$ and $b^1\Sigma$states. [b] O_2(E2) = $O_2(B^3\Sigma)$ and higher triplet states.

Table 4. Major neutral reactions included in the model.

Reaction	Rate coefficient[a]	Ref.
$O + N_2 \rightarrow NO + N$	$3.0 \times 10^{-10}\exp(-38370/T_{gas})$	[61]
$O + NO_2 \rightarrow NO + O_2$	$6.51 \times 10^{-12}\exp(120.03/T_{gas})$	[84]
$N + NO \rightarrow O + N_2$	$8.20 \times 10^{-11}\exp(-410.03/T_{gas})$	[85]
$O + NO \rightarrow NO_2$	$3.02 \times 10^{-11}\exp(T_{gas}/298.0)^{-0.75}$	[84]
$N + O_2 \rightarrow NO + O$	$4.47 \times 10^{-12}(T_{gas}/300)\exp(-3270.0/T_{gas})$	[86]
$NO_3 + NO \rightarrow NO_2 + NO_2$	1.70×10^{-11}	[64]
$N + NO_2 \rightarrow NO + NO$	2.30×10^{-12}	[64]
$N + NO_2 \rightarrow O + N_2O$	1.40×10^{-12}	[85]
$NO_2 + NO_2 \rightarrow NO_3 + NO$	$4.5 \times 10^{-10}\exp(-18500.0/T_{gas})$	[61]

[a] Rate coefficients are in cm^3s^{-1} or in cm^6s^{-1} for the two-body and three-body reactions, respectively; T_{gas} is the gas temperature in K.

Acknowledgements

This research was supported by the European Marie Skłodowska-Curie Individual Fellowship "GlidArc" within Horizon 2020 (Grant No.657304), by the FWO project (grant G.0383.16 N) and by the EU project MAPSYN: Microwave, Acoustic and Plasma assisted SYNthesis, under the grant agreement no. CP-IP 309376 of the European Community's Seventh Framework Program. The calculations were performed using the Turing HPC infrastructure at the CalcUA core facility of the Universiteit Antwerpen (UAntwerpen), a division of the Flemish Supercomputer Center VSC, funded by the Hercules Foundation, the Flemish Government (department EWI) and the UAntwerpen.

Conflict of interest

The authors declare no conflict of interest.

Keywords: energy efficiency · gliding arc · nitrogen fixation · nitrogen oxide · plasma chemistry

[1] B. S. Patil, Q. Wang, V. Hessel, Jüergen. Lang, *Catal. Today* **2015**, *256*, 49 – 66.
[2] N. Cherkasov, A. O. Ibhadon, P. Fitzpatrick, *Chem. Eng. Process.* **2015**, *90*, 24 – 33.
[3] http://energy.globaldata.com/media-center/press-releases/oil-and-gas/global-ammonia-capacity-to-reach-almost-250-million-tons-per-year-by-2018-says-globaldata.
[4] J. N. Galloway, *Environ. Pollut.* **1998**, *102*, 15 – 24.
[5] Y. Tanabe, Y. Nishibayashi, *Coord. Chem. Rev.* **2013**, *257*, 2551 – 2564.
[6] R. R. Schrock, *Proc. Natl. Acad. Sci. USA* **2006**, *103*, 17087.
[7] A. Anastasopoulou, Q. Wang, V. Hessel, J. Lang, *Processes* **2014**, *2*, 694 – 710.
[8] V. Hessel, G. Cravotto, P. Fitzpatrick, B. S. Patil, J. Lang, W. Bonrath, *Chem. Eng. Process.* **2013**, *71*, 19 – 30.
[9] R. H. Burris, G. P. Roberts, *Annu. Rev. Nutr.* **1993**, *13*, 317 – 335.
[10] T. Bazhenova, A. Shilov, *Coord. Chem. Rev.* **1995**, *144*, 69 – 145.
[11] M. E. Vol'pin, V. B. Shur, M. A. Ilatovskaya, *Bull. Acad. Sci. USSR Div. Chem. Sci.* **1964**, *13*, 1644.
[12] D. Rapakoulias, S. Cavadias, J. Amouroux, *Revue de Physique Appliquée (Paris)* **1980**, *15*, 1261 – 1265.
[13] I. Pollo, *Biul. Lubel. Tow. Nauk. Mat.-Fiz.-Chem.* **1978**, *20*, 102 – 108.
[14] J. Krop, I. Pollo, *Chemia* **1980**, *633*, 25 – 33.
[15] B. Mutel, O. Dessaux, P. Goudmand, *Rev. Phys. Appl.* **1984**, *19*, 461 – 464.
[16] V. D. Rusanov, A. A. Fridman, G. V. Sholin, *Sov. Phys. Usp.* **1981**, *24*, 447 – 474.
[17] A. Czernichowski, *Pure Appl. Chem.* **1994**, *66*, 1301 – 1310.
[18] A. Indarto, D. R. Yang, J. W. Choi, H. Lee, H. K. Song, *J. Hazard. Mater.* **2007**, *146*, 309 – 315.
[19] T. Nunnally, K. Gutsol, A. Rabinovich, A. Fridman, A. Gutsol, A. Kemoun, *J. Phys. D* **2011**, *44*, 274009.
[20] X. Tao, M. Bai, X. Li, H. Long, S. Shang, Y. Yin, X. Dai, *Prog. Energy Combust. Sci.* **2011**, *37*, 113 – 124.
[21] G. Petitpas, J. D. Rollier, A. Darmon, J. Gonzalez-Aguilar, R. Metkemeijer, L. Fulcheri, *Int. J. Hydrogen Energy* **2007**, *32*, 2848 – 2867.
[22] C. S. Kalra, A. F. Gutsol, A. A. Fridman, *IEEE Trans. Plasma Sci.* **2005**, *33*, 32 – 41.
[23] T. Sreethawong, P. Thakonpatthanakun, S. Chavadej, *Int. J. Hydrogen Energy* **2007**, *32*, 1067 – 1079.
[24] Y. N. Chun, H. O. Song, *Energy Sources. A* **2008**, *30*, 1202 – 1212.
[25] H. Zhang, F. Zhu, X. D. Li, K. F. Cen, C. M. Du, X. Tu, *Plasma Chem. Plasma Process.* **2016**, *36*, 813 – 834.
[26] D. R. Yang, J. W. Choi, H. Lee, H. K. Song, *J. Hazard. Mater.* **2007**, *146*, 1 – 11.
[27] S. C. Kim, M. S. Lim, Y. N. Chum, *Plasma Chem. Plasma Process.* **2014**, *34*, 125 – 143.
[28] H. Zhang, X. D. Li, F. S. Zhu, K. F. Cen, C. M. Du, X. Tu, *Chem. Eng. J.* **2017**, *310*, 114 – 119.
[29] H. Zhang, C. M. Du, A. J. Wu, Z. Bo, J. H. Yan, X. D. Li, *Int. J. Hydrogen Energy* **2014**, *39*, 12620 – 12635.
[30] A. A. Fridman, S. Nester, L. A. Kennedy, A. Saveliev, O. Mutaf-Yardimci, *Prog. Energy Combust. Sci.* **1999**, *25*, 211 – 231.
[31] A. Fridman, *Plasma Chemistry*, Cambridge University Press, New York, **2008**.
[32] R. Burlica, M. J. Kirkpatrick, B. R. Locke, *J. Electrost.* **2006**, *64*, 35 – 43.
[33] J. M. Cormier, O. Aubry, A. Khacef, in *NATO Science for Peace and Security Series A: Chemistry and Biology* (Eds.:S. Guceri, A. Fridman) Springer, Netherlands, **2008**, pp. 125 – 134.
[34] Z. Czekalska, *Arch. Combust.* **2010**, *30*, 337 – 346.
[35] Z. Bo, J. Yan, X. D. Li, Y. Chi, K. F. Cen, *J. Hazard. Mater.* **2009**, *166*, 1210 – 1216.
[36] J. Yang, T. Y. Lia, C. S. Zhong, X. X. Guan, C. Hu, *J. Electrochem. Soc.* **2016**, *163*, E288 – E292.
[37] B. S. Patil, J. R. Palau, V. Hessel, J. Lang, Q. Wang, *Plasma Chem. Plasma Process.* **2016**, *36*, 241 – 257.
[38] J. Amouroux, S. Cavadias, D. Rapakoulias, *Rev. Phys. Appl.* **1979**, *14*, 969 – 976.
[39] X. Tu, H. J. Gallon, J. C. Whitehead, *IEEE Trans. Plasma Sci.* **2011**, *39*, 2900 – 2901.
[40] X. Tu, J. C. Whitehead, *Int. J. Hydrogen Energy* **2014**, *39*, 9658 – 9669.
[41] S. Pellerin, J. M. Cormier, F. Richard, K. Musiol, J. Chapelle, *J. Phys. D* **1999**, *32*, 891 – 897.
[42] I. V. Kuznetsova, N. Y. Kalashnikov, A. F. Gutsol, A. A. Fridman, L. A. Kennedy, *J. Appl. Phys.* **2002**, *92*, 4231 – 4237.
[43] A. Czernichowski, H. Nassar, A. Ranaivosoloarimanana, *Acta Phys. Pol. A* **1996**, *89*, 595 – 596.
[44] O. Mutaf-Yardimci, A. V. Saveliev, A. A. Fridman, L. A. Kennedy, *J. Appl. Phys.* **2000**, *87*, 1632 – 1641.
[45] T. Kozák, A. Bogaerts, *Plasma Sources Sci. Technol.* **2014**, *23*, 045004.
[46] T. Kozák, A. Bogaerts, *Plasma Sources Sci. Technol.* **2015**, *24*, 015024.
[47] R. Aerts, W. Somers, A. Bogaerts, *ChemSusChem* **2015**, *8*, 702 – 716.
[48] R. Snoeckx, R. Aerts, X. Tu, A. Bogaerts, *J. Phys. Chem. C* **2013**, *117*, 4957 – 4970.
[49] S. Heijkers, R. Snoeckx, T. Kozák, T. Silva, T. Godfroid, N. Britun, R. Snyders, A. Bogaerts, *J. Phys. Chem. C* **2015**, *119*, 12815 – 12828.
[50] R. Snoeckx, S. Heijkers, K. Van Wesenbeeck, S. Lenaerts, A. Bogaerts, *Energy Environ. Sci.* **2016**, *9*, 999 – 1011.
[51] W. Z. Wang, A. Bogaerts, *Plasma Sources Sci. Technol.* **2016**, *25*, 055025.
[52] F. Richard, J. M. Cormier, S. Pellerin, J. Chapelle, *J. Appl. Phys.* **1996**, *79*, 2245 – 2250.
[53] S. Pellerin, F. Richard, J. Chapelle, J. M. Cormier, K. Musiol, *J. Phys. D* **2000**, *33*, 2407 – 2419.
[54] St. Kolev, A. Bogaerts, *Plasma Sources Sci. Technol.* **2015**, *24*, 015025.
[55] St. Kolev, A. Bogaerts, *Plasma Sources Sci. Technol.* **2015**, *24*, 065023.
[56] G. Trenchev, St. Kolev, A. Bogaerts, *Plasma Sources Sci. Technol.* **2016**, *25*, 035014.

[57] S. R. Sun, St. Kolev, H. X. Wang, A. Bogaerts, *Plasma Sources Sci. Technol.* **2016**, *26*, 015003.
[58] S. R. Sun, H. X. Wang, D. H. Mei, X. Tu, A. Bogaerts, *J. CO2 Util.* **2017**, *17*, 220 – 234.
[59] W. Z. Wang, A. Berthelot, St. Kolev, X. Tu, A. Bogaerts, *Plasma Sources Sci. Technol.* **2016**, *25*, 065012.
[60] V. Guerra, J. Loureiro, *J. Phys. D* **1995**, *28*, 1903 – 1918.
[61] M. Capitelli, C. M. Ferreira, B. F. Gordiets, A. I. Osipov, *Plasma kinetics in atmospheric gases*, Springer Berlin **2000**.
[62] B. F. Gordiets, C. M. Ferreira, V. L. Guerra, J. M. A. H. Loureiro, J. Nahorny, D. Pagnon, M. Touzeau, M. Vialle, *IEEE Trans. Plasma Sci.* **1995**, *23*, 750 – 768.
[63] V. Guerra, P. A. Sá, J. Loureiro, *Eur. Phys. J. Appl. Phys.* **2004**, *28*, 125 – 152.
[64] I. A. Kossyi, A. Yu Kostinsky, A. A. Matveyev, V. P. Silkov, *Plasma Sources Sci. Technol.* **1992**, *1*, 207 – 220.
[65] A. B. Murphy, *J. Phys. D* **2001**, *34*, R151 – R173.
[66] W. Z. Wang, M. Z. Rong, Y. Wu, J. D. Yan, *J. Phys. D* **2014**, *47*, 255201.
[67] M. Appl in *Ullmann's Encyclopedia of Industrial Chemistry* Wiley, VCH, Weinheim, **2012**, pp. 139 – 225.
[68] E. D. Mccollum, F. Daniels, *Ind. Eng. Chem.* **1923**, *15*, 1173 – 1175.
[69] W. S. Partridge, R. B. Parlin, B. J. Zwolinski, *Ind. Eng. Chem.* **1954**, *46*, 1468 – 1471.
[70] M. Rahman, V. Cooray, *Opt. Laser Technol.* **2003**, *35*, 543 – 546.
[71] W. L. Chameides, D. H. Stedman, R. R. Dickerson, D. W. Rusch, R. J. Cicerone, *J. Atmos. Sci.* **1977**, *34*, 143 – 149.
[72] N. Rehbein, V. Cooray, *J. Electrost.* **2001**, *51 – 52*, 333 – 339.
[73] B. S. Patil, N. Cherkasov, J. Lang, A. O. Ibhadonb, V. Hessel, Q. Wang, *Appl. Catal. B* **2016**, *194*, 123 – 133.
[74] C. E. Treanor, *J. Chem. Phys.* **1968**, *48*, 1798 – 1807.
[75] T. L. Zhao, Y. Xu, Y. H. Song, X. S. Li, J. L. Liu, J. B. Liu, A. M. Zhu, *J. Phys. D* **2013**, *46*, 345201.
[76] J. Zhu, J. Gao, A. Ehn, Z. Li, M. Aldén, M. Salewski, Y. Kusano, *Translational, rotational and vibrational temperatures of a gliding arc discharge at atmospheric pressure air* (Eds.: R. Brandenburg, L. Stollenwerk), *14th International Symposium on High Pressure Low Temperature Plasma Chemistry: Book of Contributions*, **2014**, INP Greifswald.
[77] T. M. Grigorieva, A. A. Levitsky, S. O. Macheret, L. S. Polak, V. D. Rusanov, A. Fridman, *High Energy Chem.* **1984**, *18*, 268 – 272.
[78] B. Benstaali, D. Moussa, A. Addou, J.-L. Brisset, *Eur. Phys. J. Appl. Phys.* **1998**, *4*, 171 – 179.
[79] J. H. Yan, C. M. Du, X. D. Li, B. G. Cheron, M. J. Ni, K. F. Cen, *Plasma Chem. Plasma Process.* **2006**, *26*, 31 – 41.
[80] B. S. Patil, F. J. J. Peeters, J. A. Medrano, G. van Rooij, F. Gallucci, J. Lang, Q. Wang, V. Hessel, *Plasma nitrogen oxide production from air at atmospheric pressure using a pulse powered milli-scale gliding arc reactor*, **2016**, AIChEJ, revision submitted.
[81] W. Castle, *Int. J. Refrig.* **2002**, *25*, 158 – 172.
[82] S. Pancheshnyi, B. Eismann, G. Hagelaar, L. Pitchford, Computer code zdplaskin (University of Toulouse, LAPLACE, CNRS-UPS-INP, France) www.zdplaskin.laplace.univ-tlse.fr, **2008**.
[83] G. J. M. Hagelaar, L. C. Pitchford, *Plasma Sources Sci. Technol.* **2005**, *14*, 722 – 733.
[84] W. Tsang, J. T. Herron, *J. Phys. Chem. Ref. Data* **1991**, *20*, 609 – 663.
[85] M. A. A. Clyne, I. S. McDermid, *J. Chem. Soc. Faraday Trans. 1* **1975**, *71*, 2189 – 2202.
[86] D. L. Baulch, C. J. Cobos, R. A. Cox, P. Frank, G. Hayman, Th. Just, J. A. Kerr, T. Murrells, M. J. Pilling, J. Troe, R. W. Walker, J. Warnatz, *J. Phys. Chem. Ref. Data* **1994**, *23*, 847 – 1033.

Manuscript received: January 18, 2017
Revised: February 16, 2017
Accepted Article published: March 8, 2017
Final Article published: April 4, 2017

Electronic Supporting Information:

Nitrogen Fixation by Gliding Arc Plasma: Better Insight by Chemical Kinetics Modelling

Weizong Wang,*[a] Bhaskar Patil,[b] Stjin Heijkers,[a] Volker Hessel,[b] and Annemie Bogaerts*[a]

[a]. Research Group PLASMANT, Department of Chemistry, University of Antwerp, BE-2610 Antwerp, Belgium

[b]. Laboratory of Chemical Reactor Engineering / Micro Flow Chemistry and Process Technology, Department of Chemical Engineering and Chemistry, Eindhoven University of Technology, P. O. Box 513, 5600 MB Eindhoven, The Netherlands.

E-mail: wangweizong@gmail.com, annemie.bogaerts@uantwerpen.be

1. Treatment for the vibrational levels

Because the vibrationally excited species may play an important role in gliding arc assisted nitrogen fixation, [1] we pay special attention to their kinetics.

1.1 Electron impact vibrational excitation

Electron impact vibrational excitation is very important for populating the lower vibrational levels. We calculate the rate coefficients of this process for the lower vibrational levels of nitrogen and oxygen based on the Phelps cross sections. [2]-[3] The electron impact cross sections σ_{nm} for excitation to higher vibrational levels were obtained by the Fridman approximation from the known cross section σ_{01} for excitation from the ground state to the first vibrational state. [1]

$$\sigma_{nm}(\varepsilon) = \frac{\exp(-\alpha(m-n-1))}{1+\beta n}\,\sigma_{01}(\varepsilon + E_{01} - E_{nm}) \qquad \text{(S1)}$$

Where $E_{01} = E_1 - E_0$ and $E_{nm} = E_m - E_n$ are the corresponding excitation threshold energies. Thus, the Fridman approximation shifts the cross sections on the energy scale to account for the change in the threshold energy and it scales the magnitude of the cross sections according to two parameters, α and β. As suggested in [1], For N_2, we use α = 0.7 and β = 0.05 and a recommended value of α = 0.7 for O_2 is used. Due to lack of data for excitation from O_2v1 to higher levels, we have no information on the β value and for simplicity, we set β = 0, i.e. the cross section σ_{12} has the same magnitude as σ_{01}.

The superelastic vibrational collisions may play an important role in the determination of the electron energy distribution function (EEDF). Therefore, the cross sections for electron impact de-excitation are determined from the excitation cross sections by the detailed balancing principle. [4]

1.2 Vibrational energy exchange reactions

In vibrational energy exchange reactions, the vibrational energy is either lost to translational degrees of freedom (VT relaxation) or exchanged among two molecules in the same mode of vibration (VV relaxation). The rate coefficients for VT relaxation of the N_2 and O_2 vibrational levels

with either O_2 or N_2 are determined with the forced harmonic oscillator (FHO) model, [5]-[6] which compares well with exact quantum methods. [7]

The vibrational–vibrational (VV) relaxation process is very important as it populates the higher vibrational levels out of the lower levels, which are populated by electron impact excitation (see above). The rate coefficients for VV relaxation between two O_2 levels or between two N_2 levels, as well as their combinations of VV relaxation (i.e., N_2–O_2) are again calculated with the FHO model. [5]-[6] The details about the VT and VV relaxation processes and the corresponding rate coefficients can be found in the supporting information of the reference [8].

1.3 Chemical reactions of the vibrational levels

The vibrational levels can undergo the same chemical reactions as the ground state molecules, but the vibrational energy can help to lower the energy barrier of the reaction and thus increase the reaction rate constant. To account for this in the model, we calculate their rate coefficients from the corresponding rate coefficients of the collisions from the ground-state species by multiplying with an exponential factor:

$$k(E_v, T_g) = A_0 \exp(-\frac{E_a - \alpha E_v}{T_g}) \quad \text{(S2)}$$

where A_0 is the pre-exponential factor, E_a is the activation energy of the reaction, T_g is the gas temperature, E_v is the energy of the vibrational level and α is a parameter determining the efficiency of lowering the reaction barrier by vibrational excitation.

We set the values of α for each reaction following the same assumptions as described by Fridman, [1] i.e.

- For exothermic reactions with practically no activation energy, we use α = 0.
- When no bond breaking occurs, α is taken equal to a very low value (0.015).
- When bond breaking occurs in the vibrationally excited species, α is taken as 0.9.
- When in addition to the bond breaking also an atom is transferred, α is taken as 1.0.

2. Description of the gliding arc setup in the model

Although we use a 0D model, the latter can still account for the spatial dependence of the NO_x synthesis in the GA reactor, by making smart assumptions, based on the information obtained from our experiments. These assumptions will now be explained.

High speed imaging of the GA indicates that the discharge forms a plasma column connecting the electrodes, by self-initiation in the upstream narrowest gap. Subsequently, this column is dragged by the gas flow toward the diverging downstream section. The arc grows with rising interelectrode distance until the peak applied voltage in one half cycle reaches the breakdown voltage at the shortest gap separation. Subsequently, a new arc is ignited at the shortest gap and the old gliding arc extinguishes. During the gliding arc propagation stage, the arc spots move along the electrodes with only a small deformation of the plasma column. A similar behavior was also observed in literature. [9] The plasma channel can be seen as part of a circle (see figure S1) having its centre in the middle of the shortest electrode gap (see point C in figure S1).

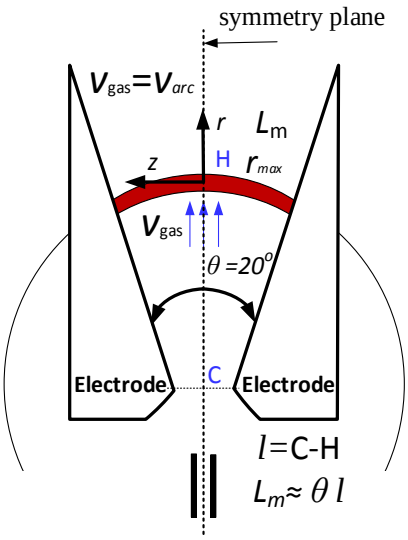

Figure S1. Schematic diagram of a moving arc between both electrodes, with explanation on how this is translated into the model. See text for explanation.

The gliding arc velocity v_{arc} as a function of axial position in the reactor was obtained by the high speed camera, and is presented in figure S2. For a gas flow rate of 2 L/min and a SEI of 1.4 kJ/L (or 0.35 eV/molec), used in the simulations, and based on the velocity distribution presented in figure S2, we can deduce the experimental gliding arc cycle (i.e., total processing time) as 4.16 ms, yielding a calculated gliding arc propagation height of 39.5 mm (see figure S3 below), which is in satisfactory agreement with the experimental data of 38.5 mm. A higher discharge power leads to a larger gliding arc propagation height and gliding arc processing time. Therefore, in order to obtain the arc velocity also at higher axial positions beyond 40 mm, we also performed high speed camera measurements at higher discharge powers, and the results are also included in the velocity distribution plotted in figure S2, because we may assume that the discharge has negligible influence on the flow field and the arc velocity is equal to the gas flow velocity. This assumption is justified when the gas flow rate and discharge power are relatively low. [10]

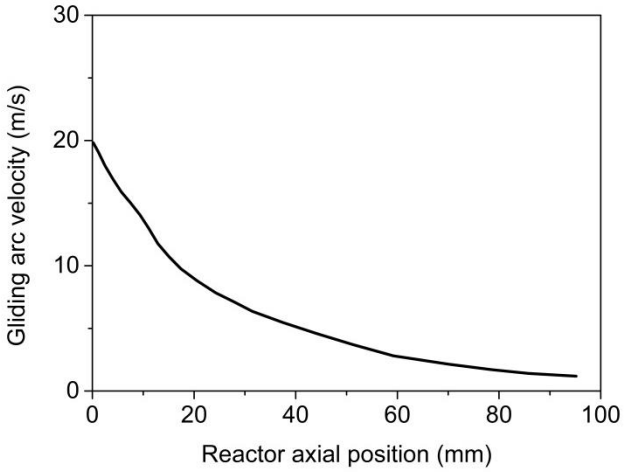

Figure S2. Measured gliding arc velocity as a function of the axial position along the symmetry plane in the reactor, for a gas flow rate of 2 L/min. 0 mm denotes the axial position at the shortest electrode separation. The end of the electrodes is at an axial position of 195 mm.

Considering that the gliding arc column can be assumed as part of a circle having its centre in the middle of the shortest electrode gap (see figure S1), we can determine the length of the gliding

arc discharge channel L_m, at different times. Indeed, for a large enough gliding arc height *l*, i.e. the distance between points C and H in figure S1, being the axial positions of the arc channel central points on the symmetry plane at the shortest interelectrode distance and the actual position, respectively, we can write: $L_m \approx \theta l$, with θ = 20° ≈0.35 rad is the angle of the electrodes with respect to each other. Subsequently, we can determine the effective gliding arc volume at each time instant, using a time-averaged apparent discharge channel radius (r_{max} = 0.5 mm) obtained by the high speed camera images. The effective gliding arc volume rises from 1.02 mm^3 at the shortest electrode gap, to about 10.8 mm^3 just before the arc extinguishes.

In the model, we assume that the gas velocity v_{gas} is equal to the gliding arc velocity v_{arc}. This means that there exists no relative velocity and only the gas within the effective gliding arc volume is processed. As a result, the real residence time of the treated gas is equal to the gliding arc cycle, and in the simulations, the local species concentration and conversion degree within the gliding arc channel should subsequently be scaled to the overall gas flowing into the reactor within the gliding arc cycle, to obtain the overall values. Indeed, the fraction of the gas passing through the arc is approximately 7.8% of the total gas flow. It is clear that the discharge volume is increasing due to the arc elongation caused by the gas blast when the arc moves downstream from the shortest gap separation. This means that the species concentration is diluted by the fresh gas N_2/O_2 entering the discharge channel, hence redistributing the species over a larger volume. At each time step during the simulation, the particle densities are corrected to account for this effect. In total, the fresh gas entering the discharge channel during the whole gliding arc cycle is about ten times the gas treated by the arc from the start.

Experimental investigations from literature indicate that the gliding arc discharge includes an initial quasi-equilibrium zone, with quasi-equilibrium temperature of 3000 to 6000 K, and a non-equilibrium zone with gas temperature ranging from 1500 K to 1000 K. [9] The non-equilibrium phase is considerably longer than the equilibrium phase, and consumes up to 90% of the total discharge energy. Due to the very high discharge frequency used in our experiments, the equilibrium phase should be very short, i.e., in the order of 10-30 ns with a high magnitude of current (~25 A) passing the reactor as observed by our experiments. Therefore, we can ignore the equilibrium stage and assume that the gas temperature decreases linearly from 1500 K at the moment of arc ignition to 1000 K when the end of the gliding arc cycle is reached (see figure S3). Once the arc extinguishes, the discharge channel arrives in a relaxation stage. We apply a temperature decreasing rate of dT/dt =-10^7K/s to describe the arc quenching process by gas convection till a gas temperature of 400K is reached. This constant temperature of 400 K is maintained in the relaxation stage, until 5 ms, which corresponds to an axial position of 44.5 mm. At this time, we stop our calculations, because the gliding arc is fully extinguished and no NO_x synthesis takes place anymore. At each time step during the simulation, the particle densities are corrected to maintain a constant pressure and to account for the effect of the gas temperature variation.

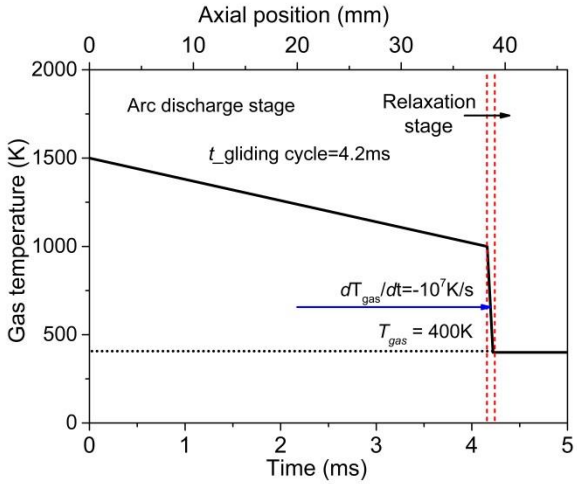

Figure S3. Gas temperature profile as a function of time and position in the reactor (see bottom and top x-axis, respectively), for a gas flow rate of 2 L/min and a SEI of 1.4 kJ/L (or 0.35 eV/molec), used in the simulations, based on the experiments of [9].

To match the conditions of a high frequency gliding arc discharge, a number of characteristic discharge pulses were implemented in the model per gliding arc cycle. Based on the typical measured voltage/current waveform and corresponding power deposition shape of one gliding arc discharge cycle, as plotted in figure S4, we implemented a simple triangular power deposition pulse every half discharge cycle, as illustrated in figure S5.

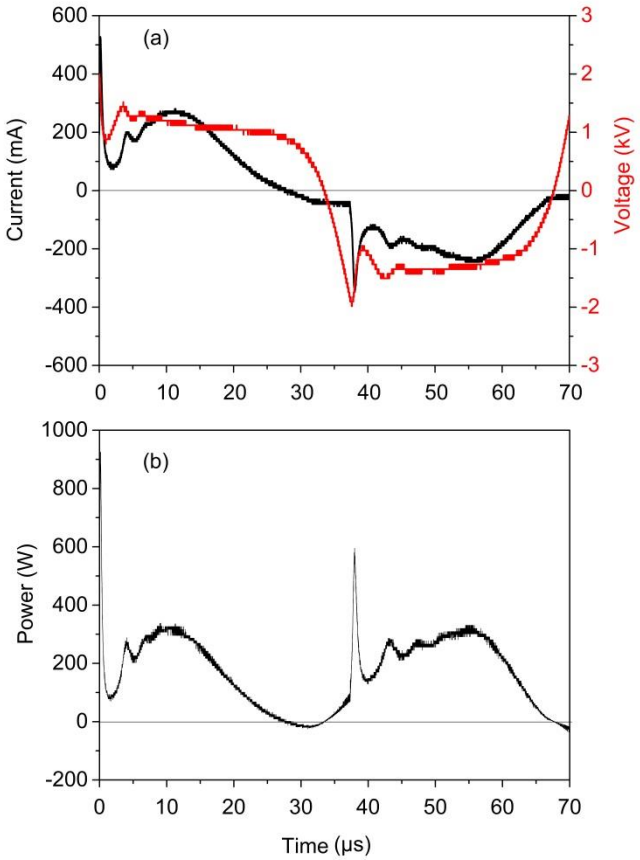

Figure S4. Applied voltage and corresponding discharge current (a), and resulting plasma power (b), as a function of time for one discharge cycle, for a gliding arc operating at 14 kHz frequency of the applied voltage, a SEI of 1.4 kJ/L and a gas flow rate of 2 L/min.

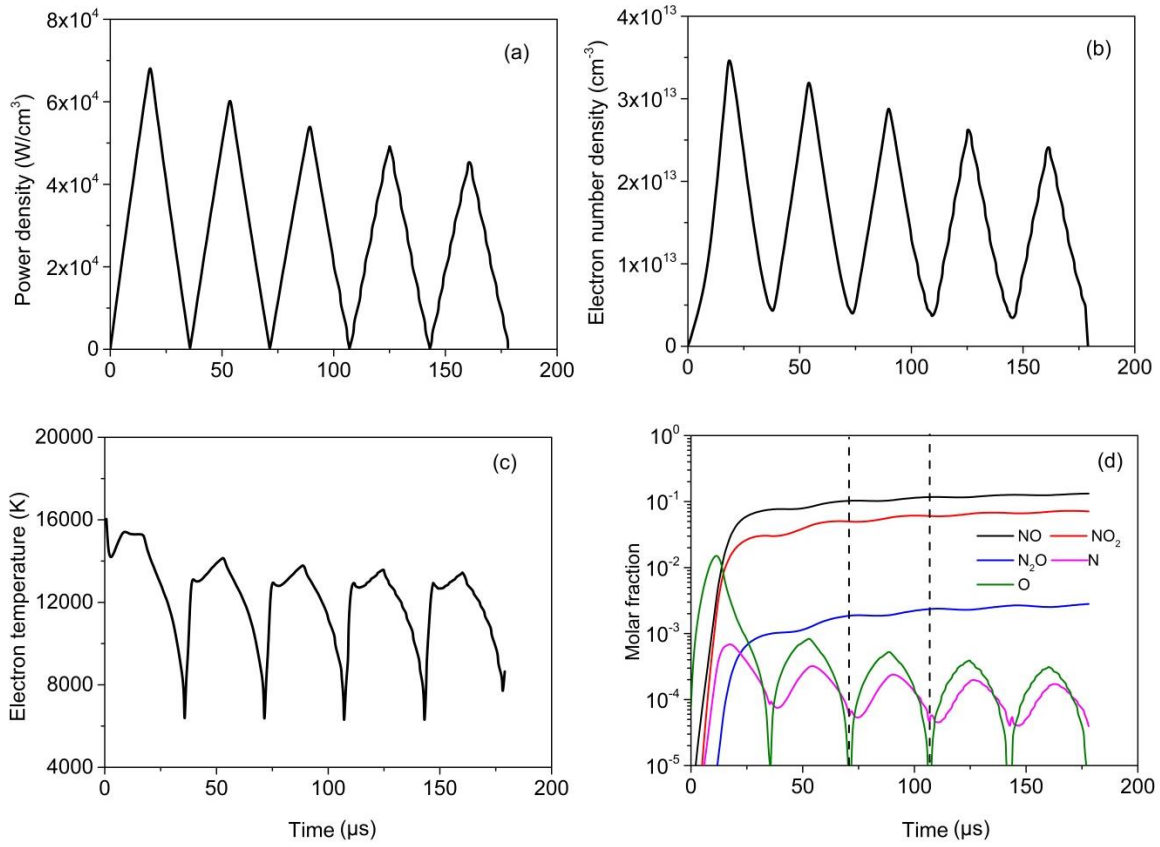

Figure S5. Applied power density (a), and calculated electron density (b), electron temperature (c), and species concentrations (d) inside the arc, as a function of time for five consecutive pulses, for a gliding arc operating in a mixture of 79% N_2 and 21% O_2. Note that a pulse in the model corresponds to a half cycle of the applied voltage, as depicted in figure S4.

Figure S5 presents the applied power density, and the calculated electron density, electron temperature and species concentrations as a function of time in five consecutive power deposition pulses (i.e., 2.5 discharge cycles). Note that one complete gliding arc cycle (i.e., 4.16 ms), comprises 58 discharge cycles, or 116 power deposition pulses. In our simulation, we assume the total power deposited in every half cycle to be constant with a time averaged value, as obtained from the experiments. As a result, the power density and hence the maximum electron density and electron temperature are decaying, as observed in figure S5, because the effective gliding arc volume is increasing very rapidly due to the arc elongation, as explained above. The decreasing trend of the maximum electron density and electron temperature are also qualitatively justified by the experiments of [9].

Our simulation predicts a maximum electron density of 3.5×10^{13} cm^{-3} and a maximum electron temperature of 15086 K, or 1.3 eV, as shown in figure S5 (b,c). Furthermore, the electron temperature in the whole gliding arc cycle is calculated to be around 11605 K, or 1.0 eV, and the peak electron density in each power deposition pulse is within the range from 1.0×10^{12} cm^{-3} to 3.5×10^{13} cm^{-3}. These values correspond well to the experimental data for low current air gliding arc discharges, [9] although it should be mentioned that it is not easy to compare different gliding arc setups with different reactor geometries and discharge conditions.

From figure S5(d), we can see that the NO_x (i.e., NO + NO_2) concentrations within the plasma volume increase very rapidly in the first half of the first arc discharge cycle. Subsequently, the NO_x concentrations only gradually rise further, because the chemical reactions contributing to the destruction of NO_x also come into play (see below). For one total gliding arc cycle, a total NO_x concentration as high as 20 % can be reached. Atomic O, important to initiate the production of NO_x, is present in significant amounts for the first half cycle, but its maximum density decreases due to its recombination with NO into NO_2. The overall concentration of N atoms is very limited, because it easily reacts with NO forming N_2. Finally, N_2O has a very minor concentration in the whole gliding arc cycle compared with NO and NO_2. This is in agreement with our experimental investigations.

3. Calculation method of thermal NO_x formation and energy efficiency by the thermal process

In order to evaluate the performance of our gliding arc for nitrogen fixation, we compare the results with the thermal NO_x yield, calculated as a function of gas temperature.

The thermal NO and NO_2 yield are calculated as

$$X_{NO}(T_g)(\%) = \left[\frac{n_{NO}(T_g)v(t)}{2n_{N2}(298K)v(0)}\right] \times 100\% = \left[\frac{n_{NO}(T_g)}{2n_{N2}(298K)}\frac{\rho(298K)}{\rho(T_g)}\right] \times 100\%$$

$$X_{NO2}(T_g)(\%) = \left[\frac{n_{NO2}(T_g)v(t)}{2n_{N2}(298K)v(0)}\right] \times 100\% = \left[\frac{n_{NO2}(T_g)}{2n_{N2}(298K)}\frac{\rho(298K)}{\rho(T_g)}\right] \times 100\% \quad \text{(S3)}$$

where n_{NO} and n_{NO2} are the number densities of NO and NO_2, respectively, and v is the gas velocity. During the derivation of equation (S3), a constant mass flow rate $Q_m = \rho(t)v(t)$ is assumed. Furthermore, we assume that the initial temperature of the gas is 298 K and the gas temperature reaches T_g at a time t. ρ is the mass density of the gaseous mixture.

The total thermal NO and NO_2 yield is then calculated as

$$X_{NOx}(T_g)(\%) = X_{NO}(T_g)(\%) + X_{NO2}(T_g)(\%) \quad \text{(S4)}$$

The specific energy input (SEI; expressed here in J) is evaluated in this case as the specific enthalpy change of the mixture H_{mix}(J/kg) divided by the total number of species per kilogram at the initial state n_t(kg^{-1}) when the dissociation has not yet taken place.

$$SEI(T_g) = \frac{H_{mix}(T_g)}{n_t} \quad \text{(S5)}$$

The energy efficiency of the thermal NO_x yield is calculated as:

$$\eta_{NOx}(\%) = \left(\frac{n_{mol,NO} \times H_{NO} + n_{mol,NO2} \times H_{NO2}}{H_{mix}(T_g)}\right) \times 100\% \quad \text{(S6)}$$

where $n_{mol,NO}$ and $n_{mol,NO2}$ (kg^{-1}) are the number of NO and NO_2 molecules per kilogram, respectively, H_{NO} and H_{NO2} are the NO and NO_2 formation enthalpy per molecule from molecular nitrogen and oxygen (0.94 eV, or 1.5×10^{-19} J for NO, and 0.34 eV, or 5.5×10^{-20} J for NO_2) and $H_{mix}(T_g)$ (J/kg) can be written as:

$$H_{mix}(T_g) = H(T_g) - H(298K) \quad \text{(S7)}$$

The specific enthalpy $H(T_g)$ is determined from the calculated chemical equilibrium composition using the standard well known thermodynamic formula. [11]

4. Formation and loss processes of NO and NO_2

In figure S6 we plot the time and volume integrated rates of the most important formation and loss processes for NO as a function of N_2/O_2 ratio, as well as the total formation and loss rate.

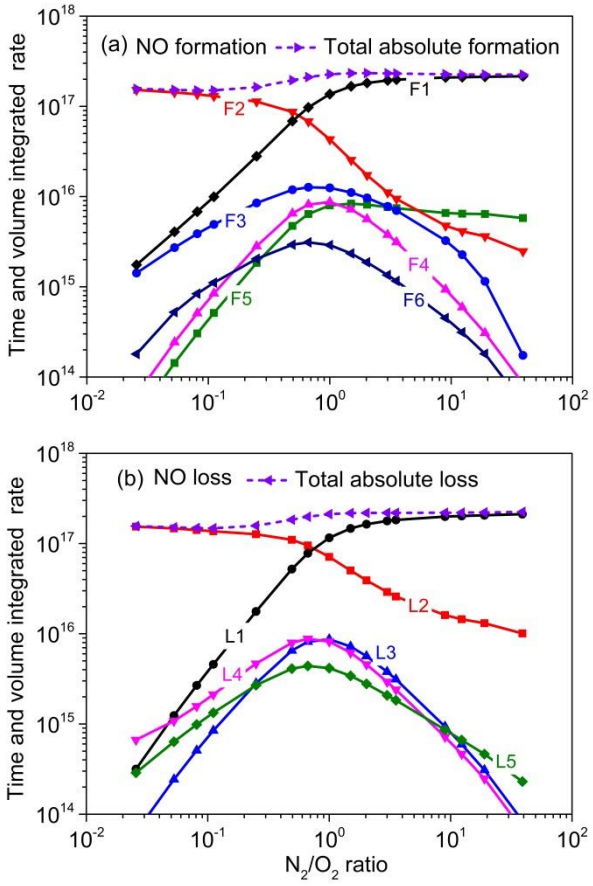

Figure S6. Time and volume integrated rates of the main formation (a) and loss (b) processes of NO as a function of N_2/O_2 ratio, for a SEI of 1.4 kJ/L (or 0.35 eV/molec), as well as the total formation and loss rate.

The formation (F1-F6) and loss (L1-L5) processes are listed in Table 1 of the main paper. Our calculations predict that the dominant reaction pathways change with increasing N_2 content. At a feed ratio of N_2/O_2 above 0.5, NO is mainly formed by the reaction of O atoms with the vibrational N_2 molecules, i.e., $O + N_2(v) \rightarrow NO + N$ (reaction F1), as a result of the reduced reaction energy barrier due to the N_2 vibrational levels. The ground state N_2 molecules hardly contribute to the production of NO, because the reaction barrier is too high. At N_2/O_2 feed ratio below 0.5, when the mixture is quite oxygen-rich, the dominant formation mechanism of NO is the reaction between O atoms and NO_2 molecules, forming NO and O_2 molecules (reaction F2). Other reactions, such as the collision between N atoms and O_2 molecules (either in ground state or vibrational levels; F3), the dissociation of N_2O_3 (F4), as well as some ion and neutral reactions (F5, F6) also contribute to NO formation, but their relative contribution is minor compared to the above mentioned two processes (not larger than 7 %). Moreover, our simulations indicate that NO formation via direct electron impact dissociation of N_2 molecules is negligible in our gliding arc, as a result of the mild discharge conditions (i.e., relatively low electron energy.

The dominant NO loss mechanism, when the N_2/O_2 feed ratio is above 1, is its reaction with N atoms into N_2 and O (L1). This indicates that quite a large fraction of NO produced by $O + N_2(v) \rightarrow$ NO

+ N (reaction F1) is destroyed by its reverse reaction. The latter greatly limits the overall NO yield and energy efficiency in the gliding arc. Hence, our calculations suggest that a key solution to increase the NO yield and energy efficiency in the gliding arc would be to avoid this reverse reaction, or to make sure that the N atoms rather react with O_2 molecules (reaction F3) than with NO, as will also be discussed below. When the N_2/O_2 feed ratio is below 1, the oxidation of NO upon reaction with O atoms, yielding the formation of NO_2, becomes most important (L2). Other loss mechanisms, such as the formation of N_2O_3 upon reaction between NO and NO_2 (L3), the reaction between NO and NO_3 forming NO_2 (L4), and the charge transfer process $NO_2^+ + NO \rightarrow NO^+ + NO_2$ (L5) also lead to the loss of NO, but only with minor relative contribution below 5%.

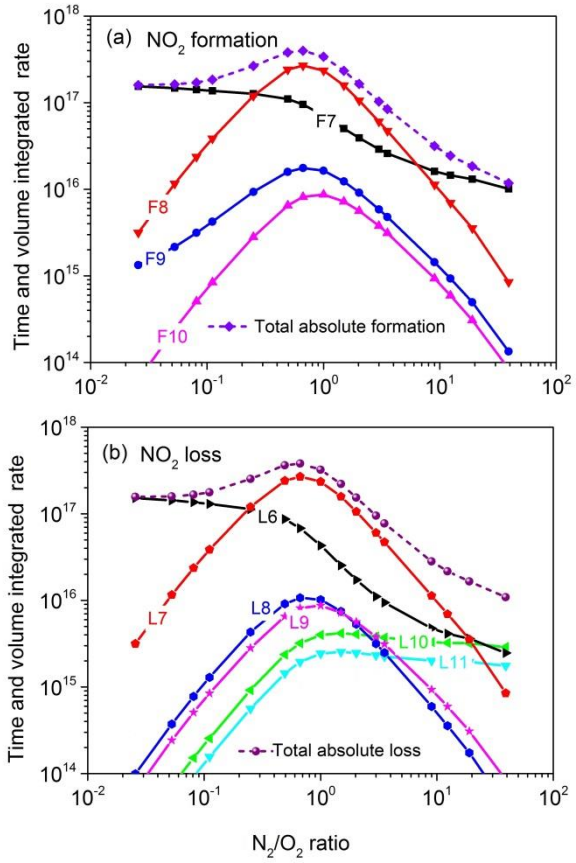

Figure S7**.** Time and volume integrated rates of the main formation (a) and loss (b) processes of NO_2 as a function of N_2/O_2 ratio, for a SEI of 1.4 kJ/L (or 0.35 eV/molec), as well as the total formation and loss rate.

Figure S7 illustrates the time integrated rates of the most important formation and loss processes for NO_2, as a function of N_2/O_2 ratio, as well as the total formation and loss rate. The formation (F7-F10) and loss (L6-L11) processes are again listed in the main paper. It is clear that the most important formation process of NO_2 at N_2/O_2 feed ratio below 0.2 and above 10 is the recombination between NO and O (reaction F7). This is also the main loss mechanism of NO at low N_2/O_2 ratio, as illustrated in figure S6 (b) above. In the intermediate range of N_2/O_2 feed ratio from 0.2 to 10, the dissociation of N_2O_4 (F8) contributes mostly to the NO_2 production, but N_2O_4 is produced by the reverse reaction of F8, and as we l show in the main paper, this reverse reaction has the same rate, so the net contribution of F8 for the formation of NO_2 is negligible. Other reactions, such as the reaction between NO_3 and NO (reaction F9) and the dissociation of N_2O_3 (reaction F10)

also yield the formation of NO_2, but their relative contribution is again very limited (not larger than 6%).

If we take a look at the loss processes, it appears that the reaction between O atoms and NO_2 (L6) is the dominant loss mechanism of NO_2 at N_2/O_2 feed ratio below 0.2, but its absolute reaction rate decreases with decreasing oxygen content in the mixture. The formation of N_2O_4 via three body recombination (L7) is the most important loss process of NO_2 when the feed ratio of N_2/O_2 is between 0.2 and 10. This is logical because in this range, the NO_2 concentration is very high (see figure 1 of the main paper). Other reactions (L8-L11) have a minor contribution to the NO_2 loss, with a maximum relative contribution no larger than 4%.

References

[1] Fridman A 2008 Plasma Chemistry (Cambridge: Cambridge University Press)

[2] Phelps database, www.lxcat.net, retrieved on January 17, 2016. Lawton S A, Phelps A V. Excitation of the b $^1\Sigma_g^+$ state of O_2 by low energy electrons. J. Chem. Phys.1978; 69: 1055-1068.

[3] Phelps database, www.lxcat.net, retrieved on January 17, 2016. Phelps A V, Pitchford L C. Anisotropic scattering of electrons by N_2 and its effect on electron transport. Phys. Rev. A 1985; 31: 2932-2949.

[4] Kozák T, Bogaerts A. Splitting of CO_2 by vibrational excitation in non-equilibrium plasmas: a reaction kinetics model. Plasma Sources Sci. Technol. 2014; 23: 045004.

[5] Adamovich I V, MacHeret S O, Rich J W, Treanor C E. Vibrational energy transfer rates using a forced harmonic oscillator model. J. Thermophys. Heat Transfer 1998; 12: 57−65.

[6] Adamovich I V, Rich J W. Three-dimensional nonperturbative analytic model of vibrational energy transfer in atom-molecule collisions. J. Chem. Phys. 1998; 109: 7711−7724.

[7] Da Silva M L, Guerra V, Loureiro J. State-resolved dissociation rates for extremely nonequilibrium atmospheric entries. J. Thermophys. Heat Transfer 2007; 21: 40−49.

[8] Heijkers S, Snoeckx R, Kozák T, Silva T, Godfroid T, Britun N, Snyders R, Bogaerts A. CO_2 conversion in a microwave plasma reactor in the presence of N_2: elucidating the role of vibrational levels. J. Phys. Chem. C 2015; 119: 12815–12828.

[9] Czernichowski A, Nassar H, Ranaivosoloarimanana A. Spectral and electrical diagnostics of gliding arc. Acta Physic A Polonica A 1996; 89: 595-596.

[10] Mutaf-Yardimci O, Saveliev A V, Fridman A A, Kennedy L A. Thermal and nonthermal regimes of gliding arc discharge in air flow. J. Appl. Phys. 1999; 84: 1062-1641.

[11] Wang W Z, Murphy A B, Yan J D, Rong M Z, Spencer J W and Fang M T C. Thermophysical properties of high-temperature reacting mixtures of carbon and water in the range 400–30,000 K and 0.1–10 atm. part 1: equilibrium composition and thermodynamic properties. Plasma Chem Plasma Process 2012; 32: 75-96.